
PHYSICS-BASED MODEL OF SOLAR WIND STREAM INTERACTION REGIONS: INTERFACING BETWEEN MULTI-VP AND 1D MHD FOR OPERATIONAL FORECASTING AT L1

A PREPRINT

R. Kieokaew* R. F. Pinto †* E. Samara ‡ C. Tao § M. Indurain* B. Lavraud ¶ A. Brunet ||
 V. Génot * A. Rouillard * N. André * S. Bourdarie ** C. Katsavrias ** F. Darrouzet ††
 B. Grison †† I. Daglis ††

March 17, 2023

ABSTRACT

Our current capability of space weather prediction in the Earth’s radiation belts is limited to only an hour in advance using the real-time solar wind monitoring at the Lagrangian L1 point. To mitigate the impacts of space weather on telecommunication satellites, several frameworks were proposed to advance the lead time of the prediction. We develop a prototype pipeline called “Helio1D” to forecast ambient solar wind conditions (speed, density, temperature, tangential magnetic field) at L1 with a lead time of 4 days. This pipeline predicts Corotating Interaction Regions (CIRs) and high-speed streams that can increase high-energy fluxes in the radiation belts. The Helio1D pipeline connects the Multi-VP model, which provides real-time solar wind emergence at 0.14 AU, and a 1D MHD model of solar wind propagation. We benchmark the Helio1D pipeline for solar wind speed against observations for the intervals in 2004 - 2013 and 2017 - 2018. We developed a framework based on the Fast Dynamic Time Warping technique that allows us to continuously compare time-series outputs containing CIRs to observations to measure the pipeline’s performance. In particular, we use this framework to calibrate and improve the pipeline’s performance for operational forecasting. To provide timing and magnitude uncertainties, we model several solar wind conditions in parallel, for a total of 21 profiles corresponding to the various virtual targets including the Earth. This pipeline can be used to feed real-time, daily solar wind forecasting that aims to predict the dynamics of the inner magnetosphere and the radiation belts.

Keywords Space weather · solar wind · corotating interaction region

1 Introduction

The Sun and the solar wind are the main drivers for space weather at Earth and in the heliosphere. Nowadays, forecasting solar wind conditions becomes a crucial task as the human society is increasingly dependent on space technologies that are under the influence of space weather. The major drivers that can have profound effects are the Coronal Mass Ejections (CMEs), caused by solar eruptions, and Corotating Interaction Regions (CIRs), formed when a fast solar

*Institut de Recherche en Astrophysique et Planétologie, UPS, CNES, CNRS, Toulouse, France (rkieokaew@irap.omp.eu)

†Département d’Astrophysique/AIM, CEA/IRFU, CNRS/INSU, Univ. Paris-Saclay & Univ. de Paris, Gif-sur-Yvette, France

‡CmPA, KU Leuven, Leuven, Belgium

§National Institute of Information and Communications Technology (NICT), Koganei, Tokyo, Japan

¶Laboratoire d’astrophysique de Bordeaux, Univ. Bordeaux, CNRS, Pessac, France

||ONERA/DPHY, Université de Toulouse, F-31055 Toulouse, France

**Department of Physics, National and Kapodistrian University of Athens, 15784 Athens, Greece

††Royal Belgian Institute for Space Aeronomy (IASB-BIRA), Brussels, Belgium

‡‡Institute of Atmospheric Physics CAS, Dept of Space Physics, Prague, Czech Republic

wind or high-speed stream (HSS) from the coronal holes takes over a slower solar wind. Although CMEs cause more severe events, their effects often disappear in a day or two while CIR/HSS events have significant effects that last several days after their arrivals [e.g. Burns et al., 2012]. During solar minima when CMEs are absent, CIRs cause low-to intermediate-strength geomagnetic storms and occasionally lead to strong geomagnetic storms [e.g. Richardson et al., 2001, Alves et al., 2006, Tsurutani et al., 2006, Zhang et al., 2008, Kilpua et al., 2017, Chi et al., 2018]. These CIR-driven storms also have impacts down to the ionosphere and thermosphere, leading to equatorial ionization anomaly [e.g. Oyedokun et al., 2022] and total electron content variability [e.g. Chakraborty et al., 2020]. Furthermore, CIRs impact the dynamics of CMEs [e.g. Liu et al., 2019], broaden solar energetic particle spectrum [e.g. Zhao et al., 2016, Wijsen et al., 2019], and modulate galactic cosmic rays [e.g. Iucci et al., 1979, Rouillard and Lockwood, 2007]. Cranmer et al. [2017], Kilpua et al. [2017], Vršnak et al. [2017], Richardson [2018] and Yermolaev et al. [2018] comprehensively reviewed our current physical understanding and the geoeffectiveness of CIRs.

Communication satellites in the geostationary orbit and medium and low Earth orbits are in the vicinity of the Earth's radiation belts - the regions encircling the near-Earth space and containing significant fluxes of high-energy electrons and ions. CIRs can drive radiation belt electron variability [e.g. Lam et al., 2009, Hudson et al., 2021], leading to electron flux enhancements [e.g. Blake et al., 1997, Li et al., 1997]; electron acceleration especially in the presence of strong southward Interplanetary Magnetic Field (IMF Bz) component [Blake et al., 1997], in which in certain cases reaching relativistic level [Paulikas and Blake, 1979, Pinto et al., 2018, Hudson et al., 2021, Pandya et al., 2019]. The high speed streams that follow CIRs have been demonstrated to be more effective (compared to CMEs) in producing multi-MeV electron enhancements up to more than 7 MeV [Horne et al., 2018, Katsavrias et al., 2019]. This is due to fact that they produce intervals of combined southward IMF and solar wind velocity over 500 km/s, which lead to an enhanced magnetic reconnection rate at the dayside magnetopause [Borovsky and Denton, 2006, Miyoshi et al., 2013].

Since the beginning of the space technology era, there have been a number of reports of spacecraft anomalies and even failures, for example, at the geostationary orbit due to the elevated fluxes of several MeV electrons that persisted for several days following CIRs [see a review by Lanzerotti, 2007]. To better mitigate impacts on those satellites, we need to develop a system for continuously predicting the solar wind and radiation belt conditions. With the real-time monitoring of the solar wind at the Lagrangian L1 point, e.g. by Advanced Composition Explorer (ACE), the continuous, real-time prediction of the radiation belt conditions via modeling is limited to one hour in advance or less as the solar wind takes about 40 - 60 minutes from the ACE spacecraft to arrive at the magnetosphere. Using the Kp that is a 3-hour index indicative of global auroral activities, the SPACECAST [Horne et al., 2013] model, for instance, was used to provide a forecast up to 3 hours in advance based on the real-time ACE data. To further improve our current capability, we need continuous solar wind prediction with a significant lead time.

Numerous efforts have been made in modeling real-time solar wind conditions at Earth. The majority of models consists of two main parts: (1) a young solar wind emergence modeling and (2) a solar wind modeling and/or propagation from near Sun to Earth. The former part is initiated by a reconstruction of the coronal magnetic fields based on synoptic or synchrone maps from ground observations; this is achieved by employing a simplified analytical model with a magnetostatic potential field source surface (PFSS) extrapolation. The PFSS extrapolation combined with the Wang-Sheeley-Arge (WSA) model is a widely-used predictor of the solar wind in the corona/low heliosphere [Arge and Pizzo, 2000, Arge et al., 2004]. In combination with the global 3-D magnetohydrodynamics (MHD) “ENLIL” — the physics-based solar wind model [Odstřil et al., 1996, Odstřil and Pizzo, 1999, Odstřil et al., 2004] — the WSA-ENLIL has been used to provide daily forecasts of solar-wind streams. The WSA-ENLIL tool has also been extended to include CMEs using an ad-hoc hydrodynamic cone model or the spheromak model [Taktakishvili et al., 2009, 2011, 2018]. The Space Weather Prediction Centre of the National Oceanic and Atmospheric Administration (SWPC/NOAA) has put the WSA-ENLIL into operation to provide daily solar wind predictions with a lead time of 1 - 4 days [Pizzo et al., 2011]. Alternative to the WSA model is the MHD Around a Sphere (MAS) that is a global, time-dependent model based on the resistive MHD equations [Linker et al., 1999, Riley et al., 2012]. The WSA-ENLIL and the MAS-ENLIL tools have been extensively benchmarked by Owens et al. [2005], Lee et al. [2009], MacNeice [2009a,b], Jian et al. [2011a,b, 2015]. For the solar-wind propagation part, several less-numerically intensive options are also available, though they are not fully put into operation at the time of this writing. A few models include Heliospheric Upwind eXtrapolation (HUX) [Riley and Lionello, 2011], ballistic propagation [Dósa et al., 2018], and Tunable HUX [Reiss et al., 2020]. MacNeice et al. [2018] and Reiss et al. [2019, 2020] compiled several combinations of the existing models and established frameworks for cross-validation.

Recently, more efforts have been made to combine and benchmark European-based models to develop operational solar-wind forecasting services. The Multi-VP is a coronal model developed by Pinto and Rouillard [2017] that computes multiple solutions of 1D solar wind flux tubes in sub-domains of interest. This approach allows a much faster calculation compared to global models with better accuracy at regions of interest, e.g. at the sub-Earth point, with a lead time of 1 – 3 days [Rouillard et al., 2020]. The Multi-VP model has been coupled with EUHFORIA [European Heliospheric Forecasting Information Asset; Pomoell and Poedts, 2018] and validated for HSS modeling in

comparison with WSA-EUHFORIA [Samara et al., 2021]. In addition, the overall performance of solar wind modeling with EUHFORIA has been assessed by Hinterreiter et al. [2019] and Samara et al. [2022]. Most recently, the HelioCast — a global MHD model comprising both coronal and heliospheric parts — has been developed by Réville et al. (under revision in JSWSC at the time of this writing) to provide a daily solar wind forecast with a lead time up to 5 days for the French organization for applied research in space weather¹⁰. Moreover, an empirical solar wind forecast [ESWF; Vršnak et al., 2007, Milošić et al., 2022] model for CIR/HSS prediction with a lead time of 4 days has been developed using an empirical relation found between the areas of coronal holes as observed in Extreme Ultraviolet data and the solar wind speed at 1 AU [Robbins et al., 2006, Vršnak et al., 2007]. This model has been put into operation by the European Space Agency.

In this work, we consider the coupling of the Multi-VP model and a 1D MHD model [Tao et al., 2005] for the first time to develop an automated pipeline named “Helio1D” for solar wind CIR forecasting. The 1D MHD model was originally developed for modeling solar wind conditions at Jupiter using the in situ observations at Earth as inner boundary; it was later extended to provide operational service for solar wind conditions at other solar-system planets [André et al., 2018], see HelioPropa¹¹. Here, we model multiple solar wind solutions at several targets around the sub-Earth point in parallel. In essence, we develop a pipeline for daily solar wind forecasting at Earth 4 days ahead with a systematic characterization of timing and amplitude uncertainties. Using 13 years of data covering parts the solar cycles 23 and 24, from 2004 to 2013 and from 2017 to 2018, we benchmark the pipeline results as well as calibrate it to develop a prototype for operational daily solar wind forecasting. The pipeline is integrated into the operational forecasting service prototype on radiation belt environmental indicators for the safety of space assets as a part of the European Union Horizon 2020 SafeSpace¹² project.

The evaluation or validation of modeling results is crucial to understand the efficiency of the forecast. Several works considered standard metrics such as root mean square, mean square error, and Pearson correlation coefficient to compare modeling results to the observations. With such metrics, a skill score is also computed to assess whether the model performs better than a baseline model. For CIR/HSS and CME modeling, some works also considered event-based verification that allow the characterization of a true positive (predicted and observed), a false positive (predicted but not observed), a false negative (not predicted but observed) to construct contingency tables [Woodcock, 1976] and compute the probability of detection [e.g. Reiss et al., 2016]. Most recently, an alternative approach using the Dynamic Time Warping (DTW) algorithm, a technique commonly employed in time-series analysis, was applied to characterize the performance of solar wind modeling [Samara et al., 2022]. We consider these metrics and approach for verification of the pipeline’s results.

The paper is organized as follows. Firstly, we introduce the Multi-VP and 1D MHD models and then describe the interfacing between them for the Helio1D pipeline. Secondly, we describe metrics and techniques for quantifying the performance of Helio1D. Thirdly, we provide results from the pipeline with the assessments of the results using the classic metrics and the DTW algorithm. Fourthly, we discuss the pipeline calibration with a newly developed approach with the DTW algorithm. Finally, we discuss operational forecasting and provide conclusions and prospects.

2 Automated CIR forecasting pipeline

We develop a pipeline to connect the solar wind forecasting from near-Sun to Earth. Here, we briefly introduce the models for the solar wind formation (Multi-VP) and solar wind propagation (1D MHD). We then describe the interfacing of the two models for the automated Helio1D pipeline.

2.1 Multi-VP

MULTI-VP [Pinto and Rouillard, 2017] is a coronal model that covers the heliocentric distances over which all solar wind streams are formed and accelerated: between 1 and about 30 solar radii (R_{\odot}). The main advantages are that it is data-driven, while taking into account the thermodynamics of the wind flows across the highly stratified low solar atmosphere, and hence it produces physically correct and realistic estimations of the state of the solar wind across its domain. MULTI-VP determines a full set of physical quantities consisting of solar-wind speed (\mathbf{V}), density (n), temperature (T), magnetic field (\mathbf{B}), and secondary quantities without requiring empirical scaling laws. In addition, MULTI-VP actually computes a set of individual wind streams from surface to high corona that can then be put together to build the full three-dimensional solar wind solutions from multiple 1D solar-wind flux tubes. This brings an enormous advantage with respect to more traditional 3D MHD models in terms of required computing time, and also by not being

¹⁰OFRAME, see <http://www.meteo-espace.fr/>.

¹¹<http://heliopropa.irap.omp.eu/>

¹²<https://www.safespace-h2020.eu/>

subject to the strong diffusion of the gradients in the transverse directions. In practice, it also lets us compute solar wind solutions restricted to certain regions of interest rather than in the full solar atmosphere.

For the 1D MHD model, MULTI-VP is required to produce time-series of the solar wind properties at the sub-Earth point at 0.14 AU (at $30 R_{\odot}$). Internally, this output is defined via a data object that lists which magnetic field lines (and hence individual wind streams) are sampled, as well as their coordinates and geometry, and properties of the input magnetogram. Each time a forecast is performed, we select a number of positions around the sub-Earth point (i.e. at 0.14 AU in Sun-Earth line) stretching up to 15 degrees in azimuth and 15 degrees in latitude. The spread in latitude is aimed to cover positional errors propagated from the magnetic field reconstruction. The spread in longitude is aimed to cover the azimuthal range that corresponds to an elemental time-series three days of solar rotation with respect to Earth, which translates to one day behind and two days ahead of the modeling at sub-Earth point. The next forecast proceeds in the same way, producing another elemental time-series that partially overlaps the previous in time. This procedure is repeated to continuously build a long-term time-series that can be used as an input to the 1D MHD model.

2.1.1 Multi-VP data

In order to characterize the pipeline performance with regard to various phases of the solar cycle, we need sufficiently long datasets. The longest historical magnetogram series available is that from the Wilcox Solar Observatory (WSO). Here, we obtain mainly two long datasets from Multi-VP processed using the WSO magnetograms. The first set extends from Carrington Rotation (CR) 2024 to CR 2139, corresponding to data from December 2004 to August 2013. This 8 year and 7 month-long interval covers the declining phase (2004 – 2008) and the solar minimum (2009 – 2010) of solar cycle 23 as well as the ascending phase (2011 – 2013) of solar cycle 24. The second set extends from CR 2192 to CR 2210 and corresponds to data from June 2017 to November 2018. These two datasets are fed into the 1D MHD model.

2.2 1D MHD model

From 0.14 AU ($30 R_{\odot}$) onwards, the solar wind is propagated through the heliosphere using a 1D MHD model [Tao et al., 2005] that takes the solar wind time-series as time-varying boundary conditions, the solar wind parameters — mainly the radial plasma velocity and tangential velocity — vary as a function of time (see more below). The 1D MHD model propagates the solar wind using an ideal MHD fluid approximation to the target position while taking into account the interaction between fast and slow streams in the radial direction. The code solves the ideal MHD equations under the influence of solar gravity in a one-dimensional spherically symmetric coordinate system. The 1D MHD equations are solved using the Coordinated Astronomical Numerical Software (CANS)¹³, an early version of CANS+ code [Matsumoto et al., 2019]. The 1D MHD code was developed by Tao et al. [2005] to propagate the solar wind observations at Earth to upstream of Jupiter, and was further extended by the French plasma physics data center¹⁴ to cover other solar-system planets or target spacecraft positions [André et al., 2018]. The code is robust and widely used for solar wind propagation and CIR modeling in the heliosphere [e.g. Palmerio et al., 2021, Nilsson et al., 2022].

The MVP output at $30 R_{\odot}$ were used as boundary conditions for the initiation of the 1D-MHD code, which then propagated these results up to the L1 point at 1 AU. The coordinate system in the 1D MHD code is equivalent to the Radial-Tangential-Normal (RTN) system, where the X -axis (R) is pointing radially outward from the Sun in the equatorial plane to the Earth, the Z -axis (N) is the solar rotation axis, and the Y -axis (T) completes the orthonormal system. The outer boundary is set to 1.4 AU where the derivatives of all physical parameters diminish. The grid spacing and the time step are chosen to be $(1.4 - 0.14)/400$ AU and 150 s, respectively. To adopt the 1D simulation, we keep the tangential magnetic field B_y component to physical values while the B_x is fixed to 0.001 nT to meet the solenoidal criterion, and the B_z is set to zero (see Tao et al. [2005] for discussion). We retrieve Multi-VP data at 30 minute cadence and resample them to 1 hour cadence; these hourly-averaged data are then linearly interpolated to meet the CFL (Courant-Friedrichs-Lewy) condition for every time step.

2.3 Helio1D - Interfacing Multi-VP and 1D MHD

To automate the interfacing between the two models, several steps are taken. Multi-VP provides solar wind time series with a full set of physical parameters including plasma number density, velocity, temperature, magnetic field in the RTN coordinates. We first format the time series to fit the input format of the 1D MHD model. Here, we take the input at a 1-hour time resolution and output the propagated time series at L1 with the same 1-hr resolution. To successfully run the 1D MHD code, two criteria are required to be met: (1) the data length must cover at least a solar rotation, i.e., 27.25 days, in order to produce a consistent CIR formation, and (2) the parameter values must be physical (e.g. non-negative

¹³developed by T. Yokoyama at the University of Tokyo and collaborators, see documentation at <http://www.astro.phys.s.chiba-u.ac.jp/netlab/pub/index.html>.

¹⁴Centre de Données de Physique des Plasmas, France. See <http://heliopropa.irap.omp.eu/>.

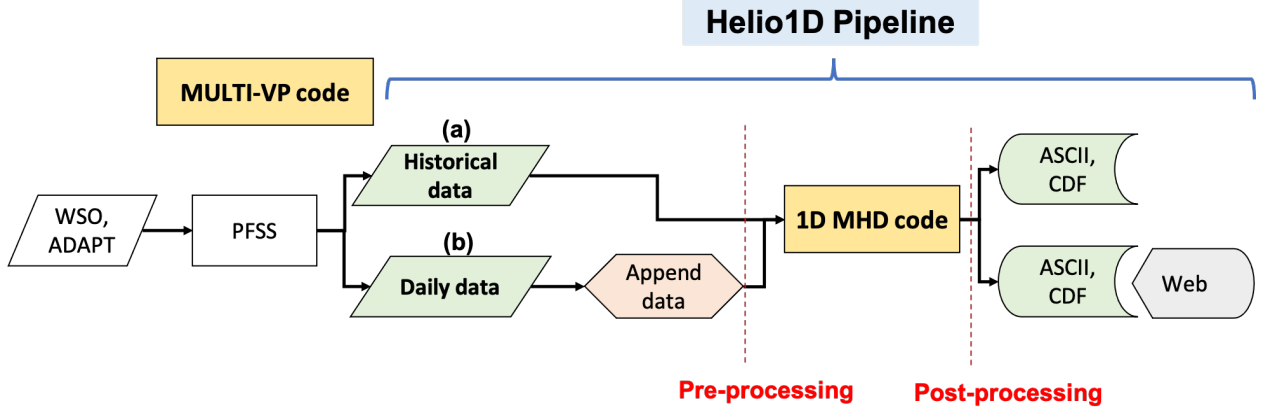


Figure 1: Diagram of the Helio1D pipeline.

plasma number density). In certain conditions, the Multi-VP model may provide unphysical solar wind values due to the poor quality of the magnetograms. We apply a set of criteria to remove unphysical values (see Appendix) and fill gaps using linear interpolation between two available data points. These aspects are further described in Section 6.

We set up the Helio1D pipeline with two modes for running (a) long-term historical data consisting of several Carrington rotations and (b) short-term data of 1-month long for daily, operational forecasting as shown in Fig 1. The mode-(a) allows us to quantify the performance of the pipeline as well as identify calibrations that may improve the pipeline performance for operational forecasting. We first benchmark the pipeline using long-term Multi-VP data in Section 4.

3 Measuring the performance of Helio1D

In this section, we first introduce the metrics and methodology for characterizing the pipeline performance. We then give results and discuss calibration for the pipeline.

3.1 Standard metrics

We choose three standard metrics - root mean square error (RMSE), mean square error (MAE), and Pearson correlation coefficient (r) - to measure the performance of the pipeline. RMSE is a classic point-by-point metric that compares the modeled value and observed value for a given point. It is defined as

$$RMSE = \sqrt{\frac{1}{T} \sum_{t=1}^T [V_m(t) - V_o(t)]^2} \quad (1)$$

where $V_m(t)$ and $V_o(t)$ are the modeled and observed values, respectively, at a given time t while T is the number of time elements. Mean absolute error (MAE) is an alternative metric that measures a similar property. It is defined as

$$MAE = \frac{1}{T} \sum_{t=1}^T |V_m(t) - V_o(t)| \quad (2)$$

where the symbols have the same meanings as defined for the RMSE. The units of the RMSE and MAE are the same as the unit of parameter values $V_m(t)$ and $V_o(t)$. Smaller values of RMSE and MAE indicate better model prediction when compared to observations. Zero values of both metrics indicate a perfect model prediction.

We also introduce the Pearson correlation coefficient (Pcc) to roughly quantify the similarities between the two time series. In principal, Pearson correlation measures the linear relationship between two datasets. Using the observed and modeled time series ($V_o(t)$ and $V_m(t)$, respectively), the formula for Pcc is

$$Pcc = \frac{\sum_{t=1}^T (V_m(t) - \langle V_m(t) \rangle) (V_o(t) - \langle V_o(t) \rangle)}{\sqrt{\sum_{t=1}^T (V_m(t) - \langle V_m(t) \rangle)^2} \sqrt{\sum_{t=1}^T (V_o(t) - \langle V_o(t) \rangle)^2}} \quad (3)$$

The Pcc -value ranges from -1.0 to 1.0 , with a value of 1.0 being a perfect positive linear correlation between the two time series and -1.0 being a perfect negative linear correlation between the two.

Additionally, to evaluate the model performance in a more concrete way using above metrics, we introduce the skill of a forecast as

$$Skill = 1 - \frac{MSE_{pred}}{MSE_{ref}} \quad (4)$$

where MSE_{pred} is the mean squared error of the prediction compared to the observation and MSE_{ref} is the mean squared error of the prediction compared to a reference baseline model. Here, we will use the average of the observation as a reference baseline model (i.e., the climatological mean in climate studies). The observations of solar wind data at L1 are taken from the High Resolution OMNIweb database [King and Papitashvili, 2005]. The average of the OMNI data of the corresponding interval are taken as a reference baseline model. Skill score equal to unity means a perfect forecast while a zero skill means that the model performs the same as the baseline model. On the other hand, a negative skill means that the model performs worse than the baseline model. The aforementioned metrics will be used throughout this report for the quantification of the performance of the model.

3.2 Dynamic Time Warping Technique

Although the classic metrics — RMSE, MAE, skill score, and Pcc — provide quantification of the performance of the model, they do not provide in-depth information such as time lags, i.e., the difference in arrival times between the modeled and observed stream interfaces, that are crucial for model evaluation. For this reason, we also consider an alternative technique called Dynamic Time Warping (DTW). The DTW technique compares two sequences by finding an optimal alignment by which one sequence may be stretched or compressed (hence, “warped”) in the temporal domain to match the other under certain constraints [e.g., Müller, 2007]. The technique was first introduced by Bellman and Kalaba [1959] in adaptive control processes and later found several applications notably in speech and pattern recognition [e.g., Sakoe and Chiba, 1978, Myers et al., 1980]. More recently, DTW has been applied in space weather in particular for comparing modeled geomagnetic indices and solar wind data to observations [e.g., Laperre et al., 2020, Owens and Nichols, 2021, Bunting and Morgan, 2022, Nilsson et al., 2022, Samara et al., 2022]. We first introduce its formulation and then describe the methodology for our application.

The DTW technique finds the warping path between two sequences, e.g., $X = \{x_1, x_2, \dots, x_{|X|}\}$ and $Y = \{y_1, y_2, \dots, y_{|Y|}\}$, through the DTW cost matrix by choosing the path that minimizes the total cumulative cost compared to all other paths. The DTW cost matrix is defined as:

$$D(i, j) = \delta(i, j) + \min\{D(i-1, j-1), D(i-1, j), D(i, j-1)\} \quad (5)$$

where i, j are the indices of X and Y , respectively, and $\delta(i, j) = |x_i - y_j|$ is the Euclidean distance between the element x_i of series X and the element y_j of series Y . Here, the optimal warping path (i.e., alignment) can be found via back-tracing in the DTW cost matrix; this process is carried out by choosing the previous points with the minimum cumulative distance [e.g., Berndt and Clifford, 1994, Keogh and Pazzani, 2001, Górecki and Łuczak, 2013]. A main disadvantage of DTW is that an element x_i may be mapped to several elements of Y — this problem is called “pathological mapping” or “singularities” [e.g., Sakoe and Chiba, 1978]. To alleviate this issue, certain constraints have been added such as the so-called windowing, slope weighting, and step patterns [see Keogh and Pazzani, 2001, and references therein]. Various variations of DTW technique have also been developed to optimize the alignments between the sequence elements/points [e.g. Keogh and Pazzani, 2001, Chu et al., 2002, Keogh and Ratanamahatana, 2005, Salvador and Chan, 2007, Efrat et al., 2007, Furtună, 2008, Zhu et al., 2012, Yadav and Alam, 2018, and references therein].

Choosing an appropriate DTW technique is crucial as different algorithms can lead to different results. Here, we choose the FastDTW algorithm developed by Salvador and Chan [2007] due to its multi-level approach. First, the time series are sampled down to a very coarse resolution. A warp path is found in this coarse resolution and projected onto a higher resolution. The warp path is then refined and projected again to a higher resolution. The process of projecting and refining is repeated until a warp path is found for the original resolution time series. Most importantly, since the technique initially finds a warp path in the coarse resolution, it is particularly appropriate to capture large-scale features in the time series, notably “CIRs” with large speed gradients.

To compute a metric similar to the skill score using the (classic) DTW technique, Samara et al. [2022] defined the Sequence Similarity Factor (SSF) to quantify the similarity between the modeled and observed time series as:

$$SSF = \frac{DTW_{score}(O, M)}{DTW_{score}(O, \langle O \rangle)} \quad (6)$$

where $DTW_{score}(O, M)$ is the DTW cost calculated between the observed (O) and modeled (M) time series, and the $DTW_{score}(O, \langle O \rangle)$ is the DTW cost between the observed series and the baseline. Here, the baseline is given as the average of the observed time series ($\langle O \rangle$). The SSF is zero when the model forecast is perfect; it equals to unity when

Table 1: List of the Helio1D long-series intervals and the point-by-point metrics calculated using the Helio1D series in comparison with OMNI data for the same intervals.

Interval	RMSE (km/s)	MAE (km/s)	FastDTW distance (km/s)	Pcc	Skill score	$SSF_{normalized}$
Jan – June 2005	175	145	89	0.05	-0.79	0.77
July – Dec 2005	179	145	105	-0.07	-1.22	1.03
Jan – June 2006	124	98	62	0.17	-1.00	0.84
July – Dec 2006	178	151	81	-0.25	-1.36	0.80
Jan – June 2007	155	125	69	0.03	-1.11	0.77
July – Dec 2007	112	94	71	0.43	-0.36	0.94
Jan – June 2008	133	108	72	-0.02	-2.24	1.16
July – Dec 2008	124	105	60	-0.03	-2.75	1.22
Jan – June 2009	91	70	55	0.10	-0.78	1.08
July – Dec 2009	75	59	42	0.12	-1.15	1.01
Jan – June 2010	103	80	67	0.32	-0.27	0.87
July – Dec 2010	142	122	108	-0.07	-1.17	1.30
Jan – June 2011	159	128	97	0.07	-0.38	0.83
July – Dec 2011	156	129	90	0.07	-0.32	0.79
Jan – June 2012	167	134	101	0.08	-0.30	0.80
July – Dec 2012	140	110	79	0.16	-0.19	0.84
Jan – June 2013	184	150	95	0.22	-0.10	0.66
July – Dec 2017	145	117	79	0.03	-1.02	0.95
Jan – June 2018	123	97	58	0.01	-0.82	0.79
July – Nov 2018	102	80	59	0.17	-0.74	0.90

the forecast performs exactly the same as the baseline; and it is higher than unity when the forecast is worse than the baseline.

The DTW cost (equation 5) calculated between two sequences is the sum of the length (i.e., the Euclidean distance) between all the optimal alignment pairs. Therefore, the existence of singularities, where a data point x_i has several possible optimal alignments to y_j , increases the DTW cost. The baseline is an average of the observed time series — it is a constant that is not varied with time for a considered interval. The DTW mapping between a model with time variation and a constant sequence (i.e., a straight line) would have several singularities. As a result, we cannot directly compare the DTW cost between two sequences with time variation to the DTW cost between a time-varying sequence and the (constant) baseline. For this reason, we propose two new metrics as follows. First, a normalized cost or normalized distance can be defined as the ratio of the DTW cost to the number of all alignment pairs. This quantity has the unit of the quantity under consideration (similar to RMSE and MAE). Its value corresponds to the average distance of all the mapped alignments that encodes both temporal and spatial differences between the two sequences; we call this quantity “DTW normalized distance”. The normalized SSF is then defined as:

$$SSF_{normalized} = \frac{DTW_{score}(O, M)/DTW_{length}(O, M)}{DTW_{score}(O, \langle O \rangle)/DTW_{length}(O, \langle O \rangle)}, \quad (7)$$

where DTW_{length} represents the number of all the alignments between two sequences. When the $SSF_{normalized}$ is smaller than unity, the forecast model performs better than the baseline. When it is less than unity, the forecast model performs worse than the baseline. We consider these two newly defined metrics besides the classic metrics in Section 4.1.

4 Results

4.1 Performance of Helio1D using the long-term data

Table 1 shows the RMSE, MAE, FastDTW normalized distance, Pcc, Skill score, and normalized SSF ($SSF_{normalized}$) from the comparison between the Helio1D and the in situ observations at L1 for each 6-month interval. The OMNI data were obtained at a 5-min resolution, and they are resampled to a 1-hour resolution to match the cadence of the Helio1D data. We find that the intervals in 2009 and the first half of 2010 have relatively low RMSE, MAE, and FastDTW distance, with the interval of July – Dec 2009 having the lowest values for all three metrics. Overall, the FastDTW

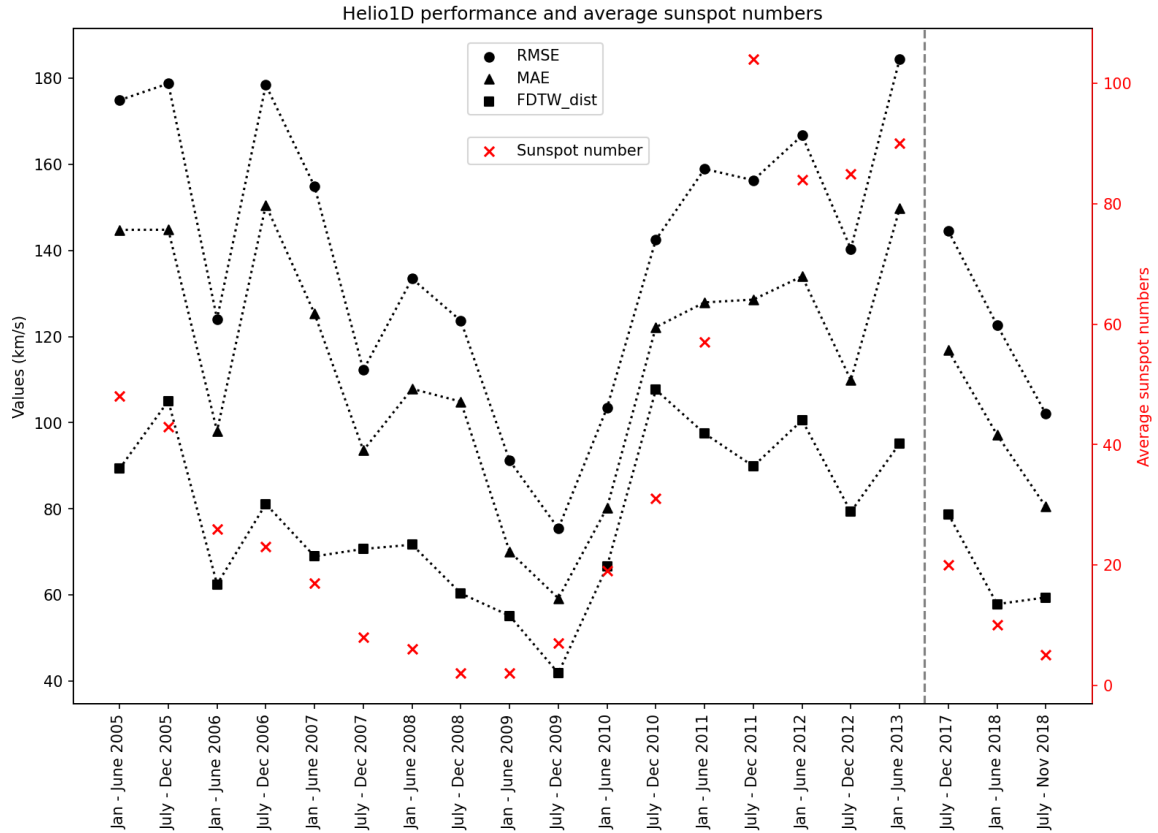


Figure 2: The average RMSE (dot), MAE (triangle), and FastDTW normalized distance (square) versus the average sunspot numbers (cross) for each 6-month interval. The values of the three metrics are shown on the left Y-axis (black) and the average sunspot numbers are shown on the right Y-axis (red). The data for 2005 - 2013 (solar cycle 23) and 2017 - 2018 (solar cycle 24) are separated by a vertical grey dashed line. The individual metric values for each solar cycle are connected by dotted lines.

distance has a lower value than RMSE and MAE for each interval. The Pcc values are mostly close to zero, and reach negative values for certain intervals, indicating that there is no linear correlation between Helio1D and OMNI data (i.e., the two data are qualitatively dissimilar). The interval of July - Dec 2007 has the best Pcc value of 0.43, showing somewhat linear correlation between the Helio1D model and the OMNI data; this interval is shown in Figure 3. The skill score is negative for all intervals, indicating that the Helio1D performs worse than the baseline model despite the relatively low errors or even positive Pcc, for some intervals. In contrast, the normalized SSF of most intervals has a value of less than unity (as highlighted in bold), indicating that the Helio1D indeed performs better than the baseline model. We discuss these different measures in Section 7. To investigate the Helio1D performance in various phases of the solar cycle, we plot these metrics against the average number of the sunspots in Figure 2.

Figure 2 shows the performance of the Helio1D characterized by the RMSE, MAE, and FastDTW distance for the intervals shown in Table 1 (left y-axis, black) compared to the average sunspot numbers of the corresponding intervals (right y-axis, red). The sunspot number data were obtained as the monthly mean total sunspot number from the Royal Observatory of Belgium¹⁵. The data in 2005 - 2013 correspond to the solar cycle 23 and the data in 2017 - 2018 correspond to the solar cycle 24. Here, we have more complete data for solar cycle 23 than the solar cycle 24. Based on the average sunspot numbers, we infer that our data for the solar cycle 23 comprise the declining phase from 2005 to 2007, the solar minimum from 2008 to mid-2009, the ascending phase from mid-2009 to 2011, and the solar maximum

¹⁵Source: WDC-SILSO, Royal Observatory of Belgium, Brussels (<https://www.sidc.be/silso/datafiles>)

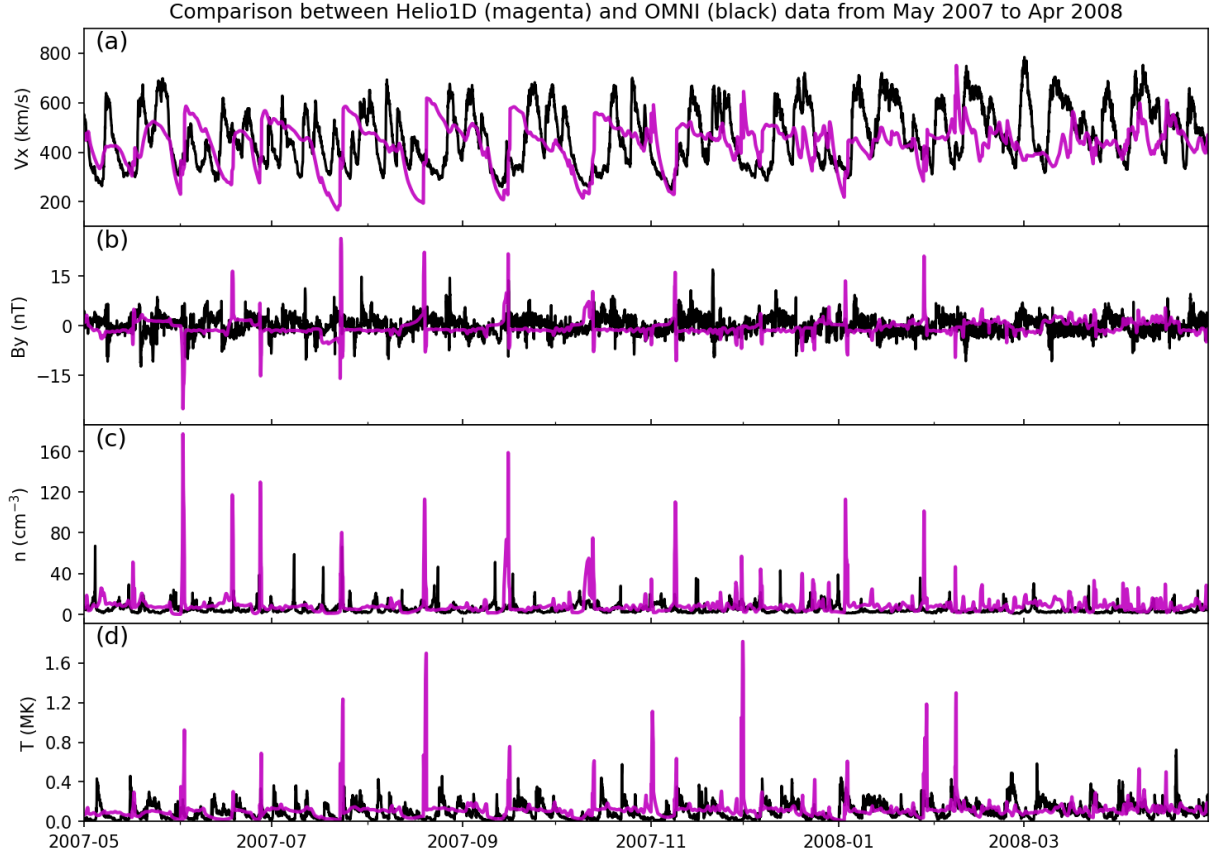


Figure 3: Comparison of CIR modeling from the 1D MHD code (magenta) to the observations (black) from the OMNI database during May 2007 and April 2008 — (a) radial bulk flow velocity (V_x); (b) tangential magnetic field component (B_y); (c) ion number density (n); and (d) ion temperature (T).

from 2012 to 2013. The rest of our data from mid-2017 to late 2018 correspond to the declining phase of the solar cycle 24.

We find that all the metric values (shown in black) vary with the average sunspot numbers (shown in red). During the declining phase of the solar cycle 23, all the metric values proportionally decrease with the average sunspot numbers. During the ascending phase of the solar cycle 23, all the metric values roughly increase with the average sunspot numbers. The most striking features are during the solar minimum and the solar maximum. The metric values reach lowest values during the solar minimum and/or the late declining phase and early ascending phase. Here we find the minimum RMSE, MAE, and FastDTW distance six months after the lowest average sunspot number in Jan – June 2009. The highest errors are found during the solar maximum, which are not surprising as the solar magnetic fields often undergo changes and they are thus less predictable. During the declining phase of the solar cycle 24, we find that the errors proportionally decrease following the average sunspot numbers. These results demonstrate that the performance of the Helio1D varies with the solar cycle — it performs best during the solar minimum and it performs worst during the solar maximum. This finding is consistent with the performance of solar wind modeling by other existing models [e.g. Hinterreiter et al., 2019]. We further discuss these results in Section 7.

To understand how the Helio1D pipeline qualitatively performs, we next visualize an example of the model output against the observations at L1. Figure 3 shows the Helio1D output in magenta and the OMNI data in black. In Fig 3a, the bulk flow velocity displays a recurring pattern of the stream interaction regions (i.e., CIRs) characterized by the transition from slow to fast wind, clearly noticeable between August and November 2007. The stream interfaces also collocate with the polarity change in B_y , shown in Fig 3b, and the enhancement of density and temperature in Fig 3c and Fig 3d, respectively. Comparing to the observations, we find that the modeled solar wind speed agrees qualitatively well and that the model correctly produces consistent CIR formation. Nevertheless, the number density and temperature

in Fig 3c and Fig 3d at the stream interfaces are generally higher than the observed values. These higher peaks are produced as a consequence of over-compression at the stream interfaces due to the ideal MHD plasma assumption in the 1D MHD code, which limits dissipation. Despite some over-compression and temporal uncertainties, we conclude that the interfacing between Multi-VP and 1D MHD works reasonably well. We further perform qualitative assessments of the pipeline performance and discuss calibration in Section 5.

From the long-term results (not shown), we find that the Helio1D pipeline correctly produces the expected large-scale modulation of CIRs especially in the bulk flow velocity, demonstrating that the Helio1D pipeline correctly produces long-term solar wind fluctuations. On a shorter timescale, there are some mismatches between the amplitudes of the fluctuations of the Helio1D results and the observations. We quantify these differences in detail in Section 4.2.

4.2 Performance of Helio1D with the FastDTW technique

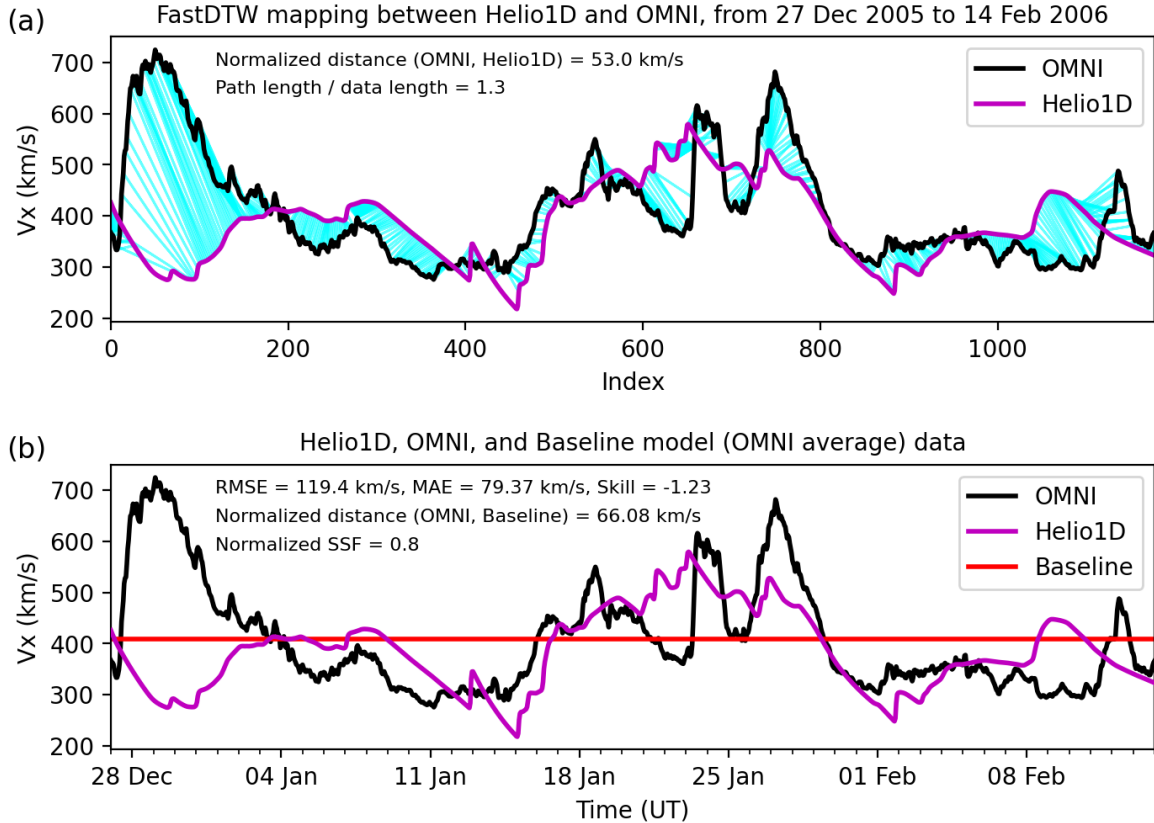


Figure 4: Example of the FastDTW mapping and performance metrics. (a) The FastDTW mapping (cyan) between the predicted CIR structures with Helio1D (purple) and the OMNI (black) data. (b) Helio1D, OMNI, and the baseline model (red) of the same interval. Relevant numbers indicative of the model performance are noted.

Since the classic metrics only indicate crude information of the model performance when comparing to real data, we consider applying FastDTW algorithm. Fig 4 shows an example of the FastDTW mapping between Helio1D and OMNI time series for the stream interfaces during 27 December 2005 and 14 February 2006. The OMNI data (black) show two clear stream interfaces and two corresponding high-speed streams. It can be seen that the Helio1D correctly produces the second stream interface along with the adjacent high-speed stream period compared to the observation despite some time delay and differences in the finer-scale structures.

Fig 4a shows the FastDTW alignments (cyan) that map large-scale features consisting in the stream interfaces and high-speed stream. The normalized FastDTW distance is about 53 km/s for this interval. As there can be several alignments for a data point (e.g., at local peaks), the number of alignment pairs is equal or larger than the length of the

data. We indicate the number of the alignment pairs (called “path length”) to the length of the data in Fig 4a. Fig 4b shows the Helio1D, OMNI, and baseline model (red) of the same interval. We note the RMSE of 119.4 km/s and MAE of 79.4 km/s, measured between the Helio1D and OMNI data. The skill score, obtained from equation 4, is -1.23 indicating that the Helio1D performs worse than the baseline model. Nevertheless, the normalized SSF (equation 7) of 0.8, obtained from the comparison of the FastDTW mapping between OMNI and Helio1D to the FastDTW mapping between OMNI and baseline model, indicates that the Helio1D model performs better than the baseline model.

This example shows that the Helio1D model prediction is still useful despite the negative skill score. We propose that the FastDTW algorithm can be used for mapping large-scale features, in particular, of the stream interfaces and high-speed streams. Here, the alignments can be used for extracting detailed information (i.e., the normalized FastDTW distance and normalized SSF) indicative of the model performance. We further exploit the alignments for model calibration in Section 5.

As illustrated in Fig 4a, the FastDTW alignments optimally match large-scale features in the time series. For a given FastDTW map path, we may define the time difference as $\Delta t = t_{OMNI} - t_{1D}$ and the velocity difference as $\Delta V = V_{OMNI} - V_{1D}$, where the subscript OMNI means the observations and the subscript 1D means the Helio1D results. Here, the statistical information on Δt and ΔV from the FastDTW mapping are useful for investigation of the model performance in terms of timing and magnitude difference. For each mapping path, $\Delta t > 0$, i.e., $t_{OMNI} > t_{1D}$, means that the Helio1D model result is ahead of the observation; while $\Delta t < 0$ means that the Helio1D model result is behind (e.g., lagged or delayed) with respect to the observation. Similarly, $\Delta V > 0$, i.e., $V_{OMNI} > V_{1D}$, means that the Helio1D model result underestimates the observed speed; while $\Delta V < 0$, i.e., $V_{1D} > V_{OMNI}$, means that the Helio1D model result overestimates the observed speed. We can measure the model performance by constructing histograms of distribution of Δt and ΔV as follows.

Fig 5 shows histograms of the Δt and ΔV of all the data obtained from FastDTW alignments on the velocity time series from 2005 to 2013. Using the Gaussian distribution fit on the histogram of Δt in Fig 5a, the median of the Δt is about 2.7 hours; the full width at half maximum (FWHM), i.e., 2.355σ , where σ is the standard deviation, is about 31.8 hours. In Fig 5b, we apply the Cauchy-Lorentzian to the ΔV distribution to extract their statistical properties as it best fits with the shape of the distribution. We find that the ΔV has the median of 0.53 km/s and the FWHM of 34.1 km/s. This means that there is almost no systematic bias for the modeling of the velocity amplitude by the Helio1D, with the majority of the modeling having ΔV within ± 34.1 km/s. In brief, considering several years of statistics covering parts of the solar cycle 23, the Helio1D model results show minimal time and velocity differences compared to the observations.

Using the FastDTW alignment information, we also explore the model performance for different types of the solar wind. In Fig 5b, for instance, we find that the ΔV distribution has slight skew or an asymmetry towards the negative values. This indicates that the Helio1D model likely overestimates the solar wind speed. To understand the model performance in detail, we consider histograms of Δt and ΔV for the individual 6-month intervals in Table 1. Particularly, we categorize the solar wind schemes into three types: (1) slow wind with $V < 400$ km/s, (2) moderate wind with $400 \leq V \leq 500$ km/s, and (3) fast wind with $V > 500$ km/s. This categorization is based on the observed solar wind. Fig 6 shows an example of distributions of Δt (a) and ΔV (b) with individual distribution fit functions to the slow (yellow), moderate (green), and fast (blue) solar winds, in addition to all solar wind (black). Table 1 in Appendix summarizes the statistical information of all the 6-month intervals.

We now discuss our fitting results to the histograms of Δt and ΔV obtained from the FastDTW algorithm in Fig 6 for the data in Jan - June, 2006. For the slow and moderate winds, the median time differences are within a few hours, with $\Delta t_{slow} = -1.5$ hours and $\Delta t_{moderate} = 3.8$ hours. For the fast wind, in contrast, we obtain a rather large time delay with $\Delta t_{fast} = 17.5$ hours. Overall, the FWHM of time delay is about 30 hours for all solar wind speed ranges. For the velocity difference, we find that the slow and moderate winds have small medians of ΔV , with $\Delta V_{slow} = 6.2$ km/s and $\Delta V_{moderate} = 3.5$ km/s. For the fast wind, however, the median of ΔV is bigger, with $\Delta V_{fast} = 74$ km/s. This example shows that the Helio1D indeed performs differently for various solar wind speed ranges. For this interval, for instance, the Helio1D model underestimates the speed of the fast wind. To investigate whether this particular behavior persists, we next consider the median Δt and ΔV of the individual 6-month intervals throughout the solar cycle 23.

Fig 7 shows bar plots of the median Δt in the left panels and ΔV in the right panels, separated for all wind types (a, b), fast wind (c, d), and slow wind (e, f). The bar plots are shown against the average sunspot numbers of the corresponding intervals to indicate the phases of the solar cycle. We note that the moderate wind does not show a particular trend and thus excluded from this plot. Overall, we find that the Helio1D has a positive Δt (Fig 7a), indicating that the Helio1D timing is ahead of the observations. The largest positive Δt is found during the ascending phase and the solar maximum (Jan - June 2012 in Fig 7a). This positive Δt is larger for the fast wind (40 hours) compared to the slow wind (25 hours) as seen in Figs 7c and 7e. For the velocity difference for all wind types, we find that the Helio1D provides a minimal velocity difference within 10 km/s except during the ascending phase and solar maximum as seen in Fig 7b.

Distributions of time and velocity differences from the DTW application of Helio1D vs OMNI from 01 Jan 2005 to 30 Jun 2013

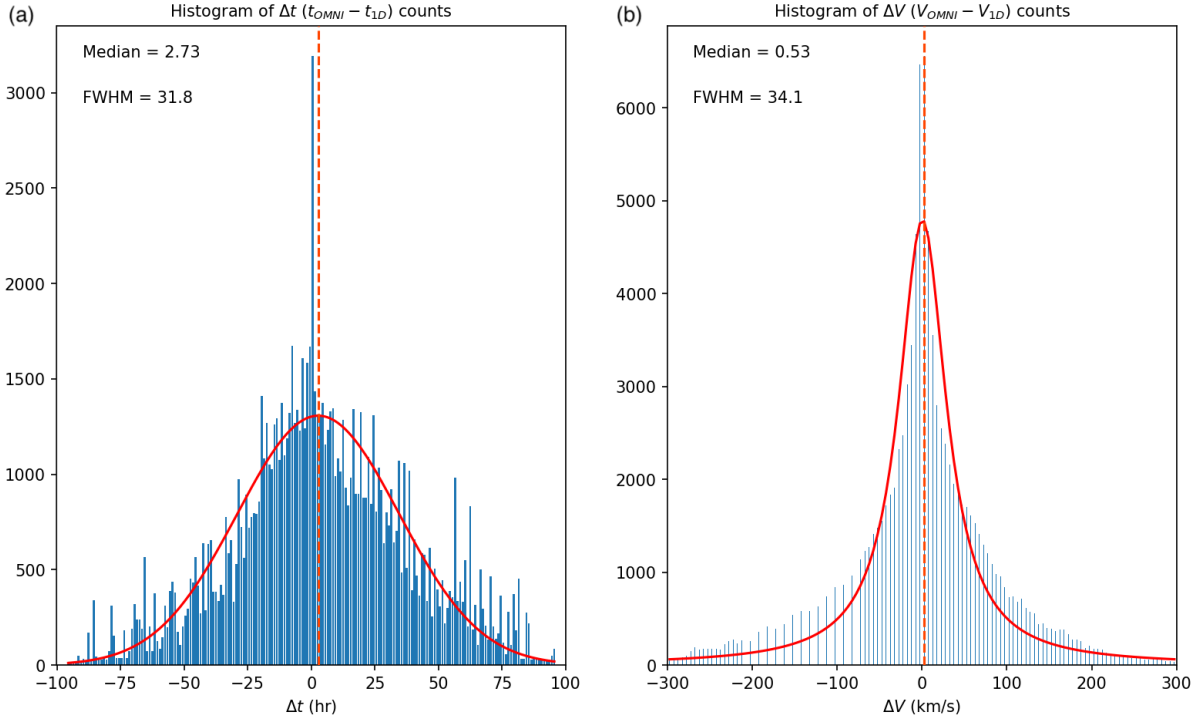


Figure 5: Histograms of (a) time delay and (b) velocity difference obtained from FastDTW alignments between the Helio1D and OMNI data from 2005 to 2018. The Gaussian (a) and the Cauchy-Lorentzian (b) distribution fits (red solid lines) are applied to obtain median (red vertical dashed line) and FWHM of the time delay and the velocity difference, respectively.

When considering the different wind types, we find that the median ΔV of the fast wind (Fig 7d) is markedly different from that of the slow wind (Fig 7f). In particular, during the solar minimum and early ascending phase, there is a large positive ΔV , indicating that the Helio1D underestimates the speed of the fast wind ($V_{1D} < V_{OMNI}$) by 50 - 150 km/s. In contrast, during the same intervals, there is mostly negative ΔV for slow wind. In other words, the Helio1D overestimates the speed of the slow wind ($V_{1D} > V_{OMNI}$). This overestimation can go up to 60 km/s as seen during the ascending phase.

In brief, we find that the timing of the Helio1D results (i.e., stream interfaces) is often ahead of the observations (consistent with Fig. 3). This positive Δt is even larger for the fast wind. In terms of the velocity, we find that the Helio1D model underestimates the fast wind speed while overestimates the slow wind speed. This effect is clear during the solar minimum and the early ascending phase.

5 Pipeline calibration

As mentioned in Section 4.1, Helio1D usually overestimates the number density and temperature of plasma at stream interaction regions as a consequence of over-compression at the stream interfaces. To alleviate this issue, we consider a post-calibration of the data to lower the extreme peaks in the Helio1D outputs. As shown in Section 4.2, FastDTW provides the alignments between the modeled and observed solar wind speeds. Since the FastDTW maps similar structures within the two time series, we create a calibration plot for the mapped values between the Helio1D and OMNI data. Fig 8 shows a kernel density estimation (KDE) plot of the mapped solar wind speeds from the Helio1D (horizontal axis) and the OMNI data (vertical axis), which shows their smoothed 2D density probability histogram. The brighter color in the plot corresponds to a higher probability density. Here, the velocity data in Fig 8a has a high probability density that mostly follows the line of slope of 1. This demonstrates that there is overall no bias from the Helio1D modeling (similar to Fig 6b), and that the magnitude of the solar wind speed from Helio1D mostly matches the OMNI data.

Distributions of time and velocity differences from the FDTW application between Helio1D and OMNI data from Jan 2006 to Jun 2006

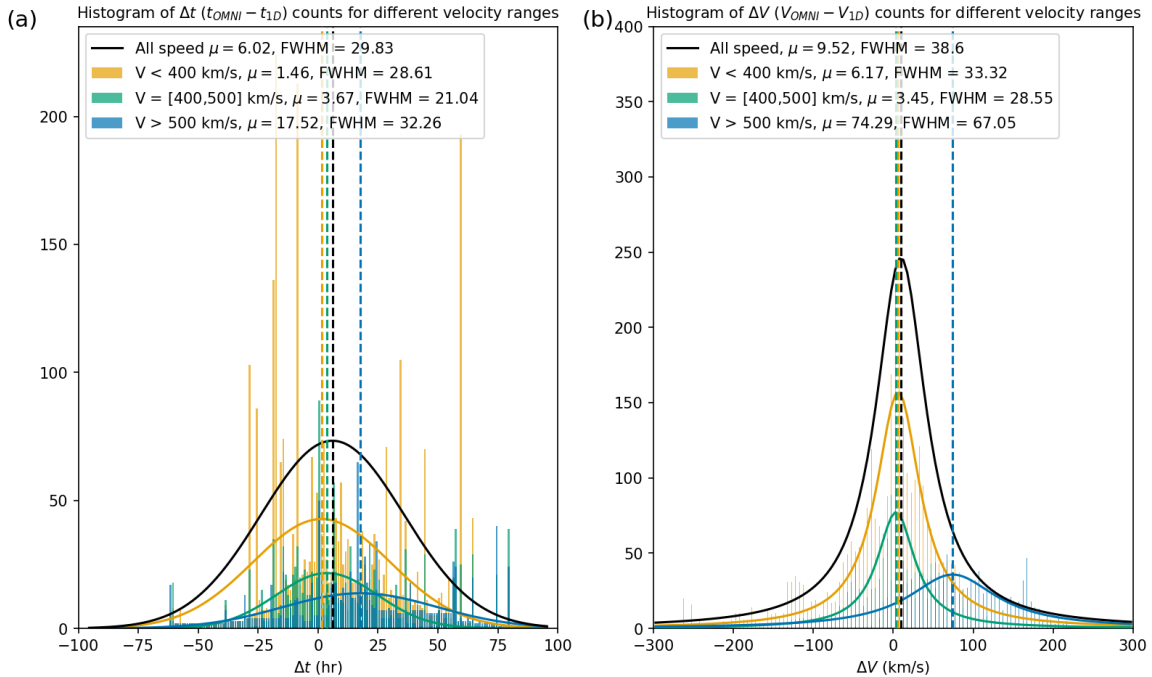


Figure 6: Histograms of (a) time delay and (b) velocity difference obtained from FastDTW alignments between the Helio1D and OMNI data from Jan to June 2006. Blue, red, and green bars represent slow, intermediate, and fast winds, respectively. (a) The Gaussian distribution fits are applied to obtain median (μ) and FWHM of the time delay. (b) The Cauchy-Lorentzian distribution fits are applied to obtain μ and FWHM of the velocity difference. The median and FWHM for all solar wind speeds are also given. See appendix for μ and FWHM all 6-month intervals.

The FastDTW alignments information allows us to map not only velocity but also plasma density and temperature values between the modeled and observed time series. In Figs 8b and 8c, we compare the plasma number densities and temperatures between the Helio1D and OMNI using the mapped path obtained from the FDTW application on the solar wind speed. It is clearly visible that the number density and the temperature from Helio1D are higher than observed values. To lessen these overestimations, we consider using linear regression. Here, we apply a linear fit onto the data shown as the red solid line in Fig 8b. Similarly, we apply a linear fit function to the plasma temperature in Fig 8c. The linear fit functions of both number density and temperature are found to have a slope of 0.653. Using these linear functions, we find that the magnitudes of the peaks of the number density and temperature better match those of the observations (not shown). We thus conclude that our calibration on the plasma number density and temperature with the linear function significantly improves the Helio1D modeling. We apply these calibrations for the number density and temperature of the Helio1D pipeline for operational forecasting described in Section 6.

6 Operational forecasting

We now shift our focus to the development of a stable “prototype” service for solar wind forecasting with Helio1D. To continuously predict solar wind conditions, several technical aspects as mentioned in Section 2.3 are addressed. First and foremost, characterization of model uncertainties is critical to assess the modeling results in order to plan for mitigation of plausible impacts of extreme events. We provide model uncertainties using an ensemble modeling in Section 6.1. Secondly, the 1D MHD model requires that the length of input time series covers at least one solar rotation in order to produce consistent CIR formation. The Multi-VP model has a setup that provides for the daily solar wind emergence comprising 72 hours of solar wind conditions covering from the present day (D) to the next two days ($D + 2$). Therefore, the solar wind emergence time series from Multi-VP must be concatenated to produce a continuous time series with a minimum length of 27.25 days. Lastly, there can be data gaps and/or unphysical values arising from either the inputs for MultiVP (i.e., magnetogram), due to the lack of data or the presence of invalid data points, or numerical errors. The implementation of automatic procedures to tackle these issues are detailed in Section 6.2.

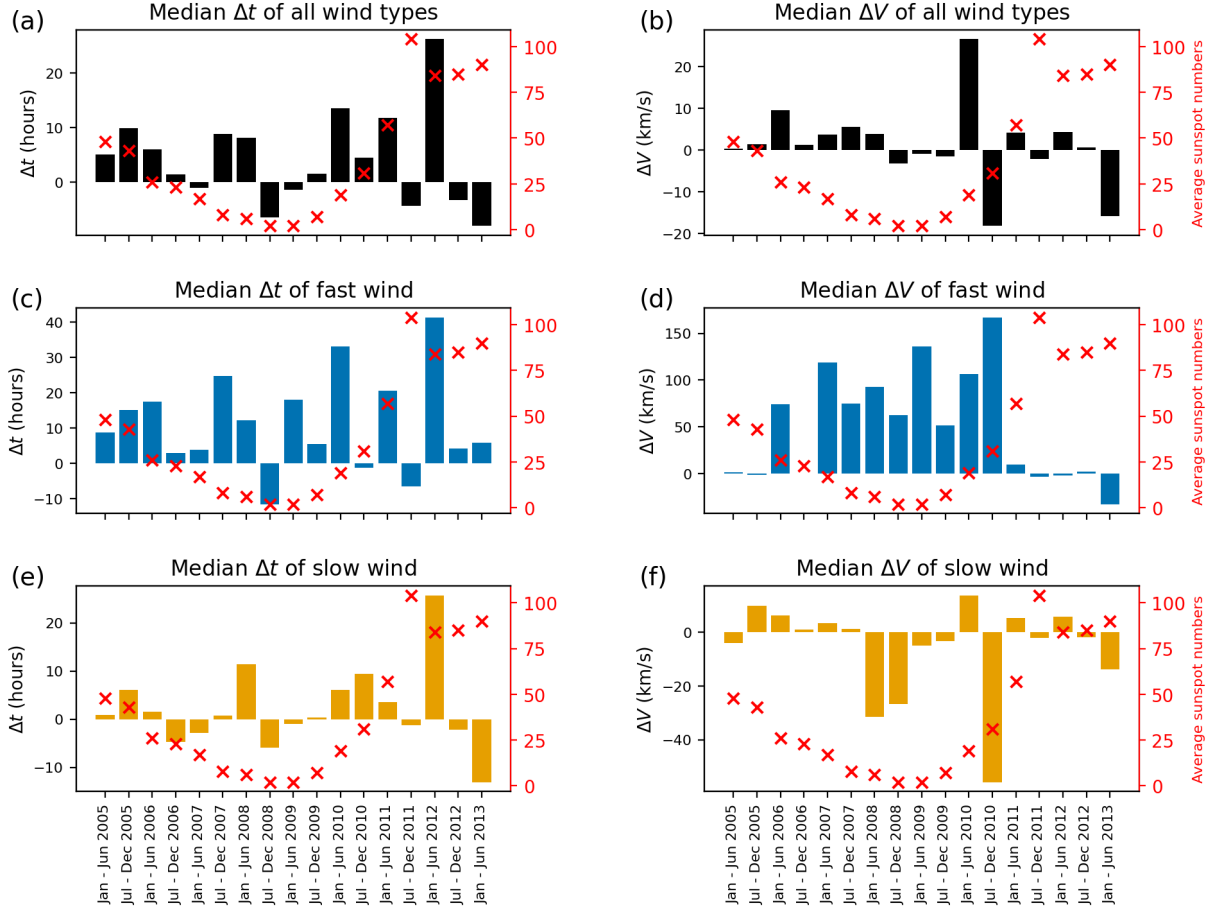


Figure 7: Bar plots of the median time difference (Δt ; left panels) and velocity difference (ΔV ; right panels) from the FastDTW technique applied to the 6-month intervals in 2005 - 2013, over-plotted by the average sunspot numbers (red cross, right Y-axis) indicative of the solar cycle. The bar plots are shown for (a, b) all wind types, (c, d) slow wind, and (e, f) fast wind.

6.1 Helio1D ensemble modeling with 21 virtual targets

We perform an ensemble forecasting of the MULTI-VP and 1-D MHD models by considering a range of heliospheric latitudinal and longitudinal uncertainties. For example, a solar wind structure that is ahead or behind in time compared to the observation can be accounted for by considering the time-series at some nearby heliospheric longitudes. Also, the magnitude of the solar wind speed profiles is different at different heliospheric latitudes as a function of the warping of the Heliospheric Current Sheet and nearby velocity gradients. Using daily magnetograms from WSO, we set up the Multi-VP model to automatically generate daily one-dimensional solar wind profiles that cover from D to $D + 2$ at the sub-Earth point and the surrounding virtual targets. The surrounding virtual targets are set to spread up to 15° from the sub-Earth point in latitude and longitude; they are set at 5° apart from each other in latitude and longitude; these chosen points constitute the star-grid pattern with the total of 21 points including sub-Earth point (see Appendix). The spatial cuts through these 21 points on the 2D map of solar wind emergence from Multi-VP along the ecliptic are then translated to temporal solar wind profiles. These 21 time-series inputs are automatically fed into the 1D MHD to propagate them in parallel from 0.14 AU to 1 AU. The 1D MHD model is rather computationally inexpensive; the model running with 21 virtual targets remains fast compared to 3D MHD modeling in general.

Fig 9 shows results from the Helio1D pipeline with the 21 virtual points between March and May, 2018. The Helio1D data at the sub-Earth point are shown in blue, and the observation data are shown in black. The green shade highlights the spread of values between the minimum and maximum among the 21 virtual targets at each hour. Panels (a) - (d) show the solar wind speed, tangential magnetic field, plasma number density, and plasma temperature, respectively. We

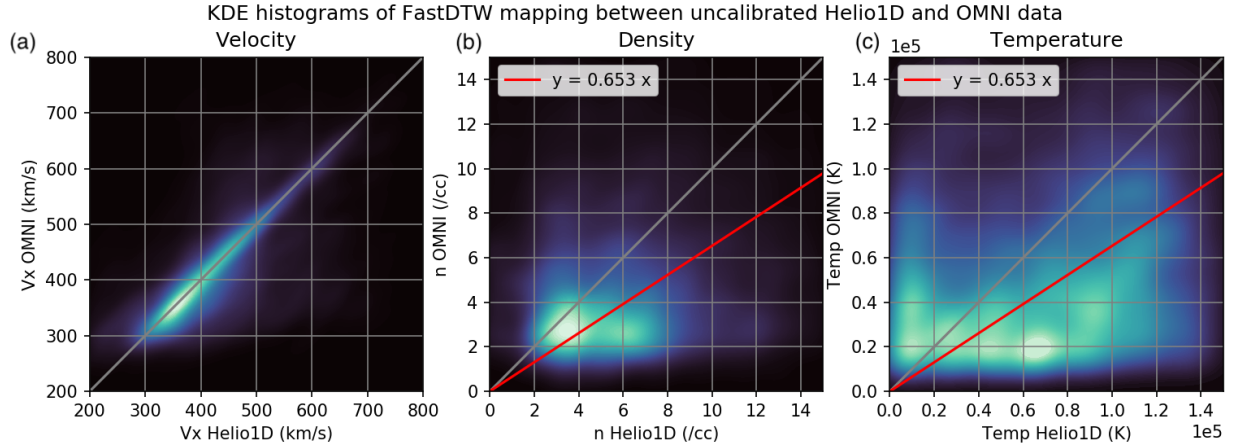


Figure 8: Calibration plots obtained from the FDTW alignments between Helio1D (horizontal axis) and OMNI (vertical axis) time series for (a) solar wind speed, (b) number density, and (c) temperature.

note that the post-calibration with the linear functions for number density and temperature (found in Section 5) has been applied. Here, the ensemble spread in green shade provides an error bar. In this example, we find that the stream interfaces modeled for the sub-Earth point appear to lag behind the observations for about two days. Nevertheless, the timing uncertainties from the values at the virtual points indeed cover the timing of the arrivals of observed stream interfaces. Overall, we find that most of the observed data points fall within the error spread for both magnitude and timing, although there are some underestimations of the speed of the high-speed stream (consistent with our findings in Section 4.2). We conclude that the Helio1D modeling using the 21 virtual targets improves the modeling compared to using only one virtual point targeting at Earth.

6.2 Solar wind data concatenation & Data gaps

The main technical problems deal with the automated interfacing between Multi-VP and 1D MHD model. Unlike the model benchmarking and case-by-case analysis, we rely on automatic modeling for both the Multi-VP and 1D MHD models. Here, the Helio1D pipeline is scheduled to run in-house every day. First, the Multi-VP is set up to produce a daily forecast with a data length of 3 days, covering from day D to $D + 2$. We first concatenate these Multi-VP data for each virtual target by averaging the data from the day $D - 30$ to the present day D to make the time series input to be sufficiently long. After the concatenation process, this 1-month solar wind profile at 0.14 AU is subsequently propagated by the 1D MHD model to provide the solar wind profile at 1 AU. Since the solar wind takes time to propagate to the Earth, we gain an extra lead time of 2 – 7 days depending on the solar wind speed. To provide a total lead time of 4-days from Helio1D, we limit the extra time gained from the 1D MHD propagation modeling to 2 days. This setup has been done to automatically interface the Multi-VP and 1D MHD to provide daily solar wind nowcast and forecast from day D to $D + 4$ (see branch (b) in Fig 1). In an absence of the magnetogram data, the magnetogram of the previous solar rotation is programmed to be fetched. This procedure is implemented based on the assumption that the coronal structures remain unchanged compared to the previous solar rotation (i.e., when the consistent, recurring CIRs are expected).

Furthermore, one of the models, or both, may terminate earlier than expected and give incomplete outputs. This is because, in reality, there can be data gaps arising from the lack of daily data (e.g., magnetogram data), or unphysical values in the data. The latter can come from numerical errors from one of the codes or poor quality of the raw inputs. To prevent the Helio1D pipeline from early termination, we perform an automatic search for data gaps and unphysical values (after performing the fetching of previous magnetogram when the present-day magnetogram is unavailable as mentioned above). The data gaps are then filled using linear interpolation between two available data points. The unphysical values identified using the criteria (see Appendix) are subsequently removed. The resulting data gaps are then filled using linear interpolation. To remove unphysical features that may arise from these procedures, we perform a running average on the data using a window of ± 3 hours centered around the data point. Finally, when either the input or daily output is shorter than expected, we fill the data with latest available values to complete the length of expected output. For practical purpose, we provide daily solar wind time series extending from day $D - 3$ to $D + 4$ for a given day D .

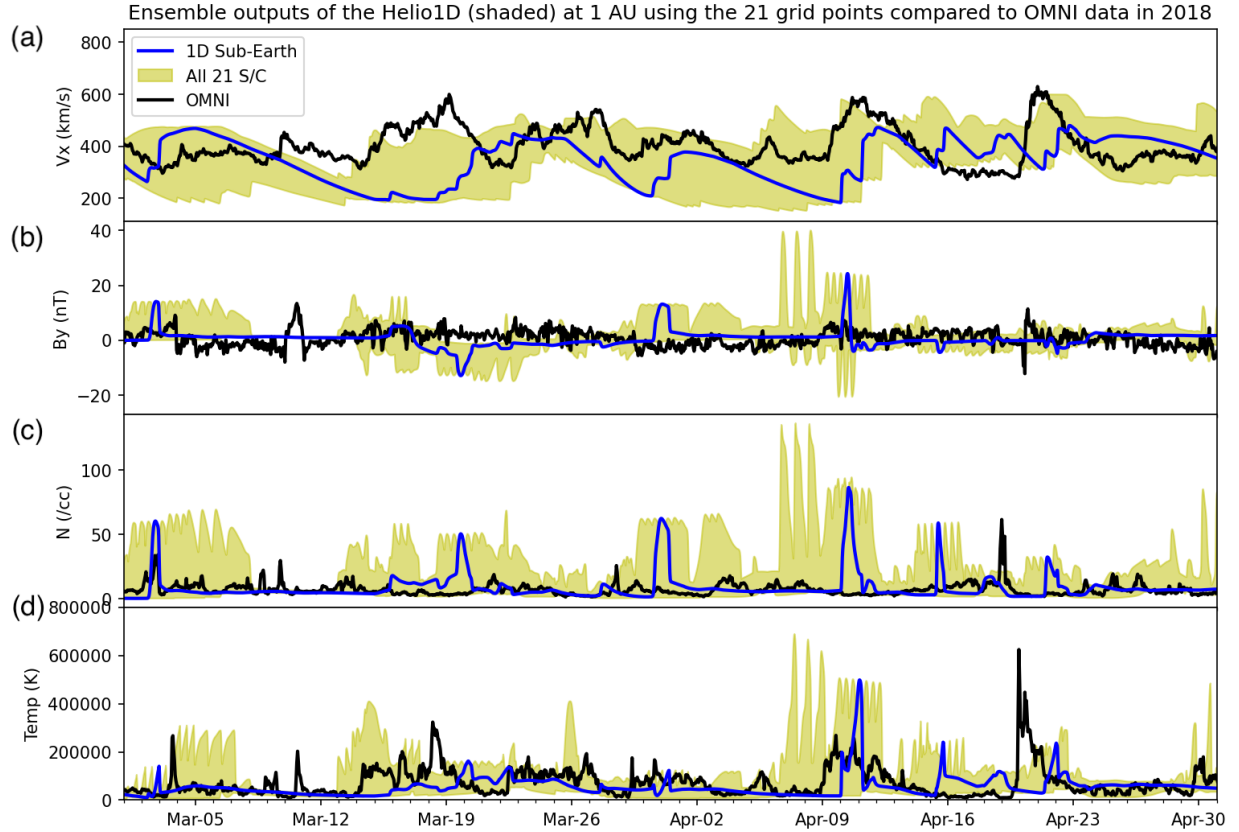


Figure 9: Helio1D ensemble time series outputs using the 21 virtual spacecraft compared to the OMNI data for March to April, 2018. The ensemble Helio1D outputs are shaded in green and the output at sub-Earth point is plotted in blue. The observation data are represented by a black line.

Example plots of the daily data from the Helio1D are publicly available; they can be accessible from <http://swift.irap.omp.eu/> and, in the near future, through the ESA Space Safety Program via www.esa.int/Space_Safety/Space_weather.

7 Discussion

We developed the Helio1D pipeline for solar wind modeling by interfacing Multi-VP for the coronal part and 1D MHD for the interplanetary part. The interfacing has been done for the first time as an effort to connect two developed models for operational forecasting purpose. Using the long-term Multi-VP data produced with the WSO magnetograms in 2005 - 2013 and 2017 - 2018, we evaluated the pipeline performance in various phases of the solar cycles 23 and 24. In addition to classic metrics such as RMSE, MAE, and skill score, we devised a new metric based on the FastDTW algorithm. Using the long-term data and the metrics, we discuss our main findings as follows.

1. The performance of the Helio1D pipeline is dependent on the phases of the solar cycle. Using the RMSE, MAE, and FastDTW distance, measured for each 6-month interval, we find that their values positively correlate with the average sunspot numbers of the previous 6-month interval. The RMSE, for example, reaches a minimum value of 80 km/s during the solar minimum, and reaches a maximum value of 180 km/s during the solar maximum. Overall, the Helio1D pipeline provides minimal magnitude errors during the late declining phase and the solar minimum.
2. The Helio1D pipeline produces consistent CIR formation. For each CIR, the solar wind speed profile at the stream interface qualitatively agrees with the observations (Fig 3a). Thus, the model sufficiently includes the large-scale physics of the CIRs. However, due to the limited dimensionality and ideal MHD assumption, the compression at stream interfaces (resulting in extreme peaks of number density and temperature) is rather

strong compared to the observations. This effect was found to be common to 1D MHD models used for solar wind propagation [e.g., Zieger and Hansen, 2008]. To alleviate this effect, we perform a post-calibration to lower the peaks at stream interfaces using a linear function. This linear function was found using the FastDTW alignments of the solar wind profiles, which particularly mapped stream interfaces.

3. Using the FastDTW alignments, we also evaluated the timing and magnitude differences between the Helio1D and the observation data. For the data in the solar cycle 23, we find minimal Δt of 2.7 hours and ΔV of 0.5 km/s. However, when separating the data into shorter intervals of 6-months and categorizing the solar wind types based on its speed, we find different results summarized as follows.
 - 3.1 For all wind types, we find that the Helio1D timing is often ahead of that of the observation for about 10 hours. This timing error is highest six months after the average sunspot number reached the maximum in late 2011. Meanwhile, the ΔV for all wind types remains low throughout the solar cycle except for the ascending phase of the solar cycle in 2010.
 - 3.2 The fast wind has higher Δt and ΔV than those of the slow wind. The Helio1D timing of fast wind is often 10 - 20 hours earlier than that of the observation, and this timing difference goes up to 40 hours six months after the highest sunspot number. For ΔV , the Helio1D pipeline mostly underestimates the speed of the fast wind for about 50 - 100 km/s during the declining phase and solar minimum; this difference goes up to ~ 150 km/s during the late ascending phase.
 - 3.3 The timing of the slow wind agrees with that of the observations within ± 10 hours, except during the solar maximum. For ΔV , the Helio1D pipeline often overestimates the speed of the slow wind for about 20 - 40 km/s. The ΔV is largest with a value of -60 km/s in late 2010.

Comparing to existing models that have been benchmarked using large data sets, the performance of the Helio1D pipeline is in agreement with other equivalent models. Owens and Riley [2017] utilized solar wind emergence at 0.14 AU from MAS based on Carrington maps (e.g., WSO) of the photospheric magnetic field. Particularly, they used a large ensemble ($N = 576$) of solar wind time series from MAS, where the ensemble members are produced from sampling solar wind solutions within a range of latitudes about the sub-Earth point. The solar wind flows at 0.14 AU are then propagated using the HUX model [Riley and Lionello, 2011] that is based on the fluid momentum equation [e.g., Pizzo, 1978] and takes into account a residual solar wind acceleration [Schwenn, 1990]. Using a long interval of data from 1996 to 2016, they find that the median RMSE of the upwind ensemble propagation is 107 km/s. Reiss et al. [2020] performed a forecasting of ambient solar wind using the WSA model and the HUX tool as well as the Tunable HUX [Reiss et al., 2020] to map solar wind flows from near Sun to Earth for the period 2006 - 2015. Their RMSE is ranging from 90 to 122 km/s while their MAE is ranging from 72 to 93 km/s. Their skill scores are negative for WSA/HUX (greater than -0.6) and positive (less than 0.06) for WSA/THUX. Compared to their studies, our Helio1D pipeline performance characterized by the average RMSE and MAE are in agreement with their models despite somewhat larger values by about a few 10 km/s. Nevertheless, RMSE and MAE are rather crude metrics; they do not tell all qualities of the prediction and the measurement, e.g., as discussed by MacNeice et al. [2018] and several others.

Regarding to the variation of the Helio1D performance with phases of the solar cycle, we find that our findings are generally consistent with other 1D MHD models. Zieger and Hansen [2008] performed an extensive validation of solar wind propagation using a 1D MHD model. They find that the variation of the coronal structure on the timescale of a solar rotation, characterized by the recurrence index of solar wind speed, plays an important role in the prediction efficiency. This explains our Helio1D results such that, in an absence of variation, i.e., during the late declining phase, the model generally predicts CIR formation consistent with the observations. In contrast, in a presence of strong variations, i.e., when there are CME emergences during the ascending phase and the solar maximum, the model generally predicts poor results compared to the observations.

In terms of timing, we find that there is a bias on the solar wind stream arrival time such that the Helio1D solar wind streams usually arrive 10 hours earlier than the observations. This bias is stronger for the fast wind compared to the slow wind. This effect may come from the assumption of an ideal MHD plasma in the 1D MHD model that ignores finer-scale physics and/or interactions that could slow down fast wind or accelerate slow wind in the interplanetary space. Moreover, the limited dimensionality of the simulation does not take into account the propagation in other directions; this may result in the timing mismatch. In terms of magnitude, the Helio1D underestimates the speed of the fast wind while overestimates the speed of the slow wind. The bias on the fast and slow wind magnitudes may come from the lack of the physics on solar wind acceleration. In HUX model, an empirical, ad-hoc solar wind acceleration is incorporated into the model [Schwenn, 1990]. Since the 1D MHD code was originally developed for solar wind propagation in the outer heliosphere [Tao et al., 2005], this physics was deemed less important and it was not added into the model. We note that this aspect must be addressed in a future improvement of the 1D MHD model for the inner heliosphere; this aspect out of scope of this work which focuses on interfacing the matured models.

Our work devised a new exploitation of the FastDTW technique for a detailed assessment of the Helio1D performance. In particular, the FastDTW alignments encoded optimal time delays and magnitude differences between the modeled stream interfaces and observed structures. We highlight that the FastDTW can be used to provide more qualitative measures than RMSE, MAE, and skill score, for example. We also demonstrated that the FastDTW (normalized) distance correlates with the RMSE and MAE. Nevertheless, the FastDTW technique is not without caveats. The main constraint of DTW techniques in general is the pathological mapping or the singularities. Therefore, the obtained Δt and ΔV from the DTW applications are not unique but instead depending on the constraints that have been added. In our case, we restrict that the alignments along the time axis must be within 96 hours (corresponding to the time that a solar wind with an intermediate speed should take to travel from 0.14 to 1 AU). Furthermore, we chose the FastDTW technique in particular because it searches to first map the structures at coarse scales, then refine to smaller scales. We emphasize that this algorithmic feature is desirable for mapping large-scale solar wind structures such as CIRs or CMEs.

Finally, we highlight the work that needs to be taken to develop an automated solar wind forecasting pipeline of Helio1D. In addition to the pipeline calibration to alleviate the pipeline caveats, there are other aspects that must be addressed. This comprises (1) providing model uncertainties and (2) dealing with data gaps and bad data. The Helio1D modeling of an ensemble of 21 solar wind solutions was shown to be a reasonable method to provide worst case scenario especially for the timing of stream interface arrivals. We note that the ensemble members can be further exploited to obtain an optimized forecast; we leave this aspect for future work. Most importantly, to develop a reliable service, we implemented strategies to tackle with data gaps and bad data points so that the pipeline can automatically run and provide continuous nowcast and forecast. This aspect should be further tested in order to evaluate their impacts on accuracy, performance, and stability of the operational forecasting pipeline. Such a task is of particular importance; it requires dedicated tests on this prototype pipeline in various situations before employing it for applications in real world.

8 Summary

We developed a prototype pipeline “Helio1D” that automatically interfaces the coronal model “Multi-VP” and the solar wind propagation model “1D MHD” to provide nowcast and forecast of ambient solar wind containing CIRs at L1. The operational prototype pipeline provides daily solar wind modeling with a lead time of 4 days. In this work, we benchmarked and extensively tested the Helio1D pipeline using 10 years of data spanning from late 2004 - 2013 and 2017 - 2018. We evaluated the performance of the pipeline using classic metrics including RMSE, MAE, and skill score. In particular, we devised a new exploitation of the FastDTW technique to map large-scale solar wind structures of CIRs. We demonstrated that this technique can be used to characterize the detailed performance of the solar wind modeling with Helio1D. For instance, we characterized the statistical information on timing and magnitude differences for velocity profiles of stream interfaces. Using this new approach, we assessed the pipeline performance for various phases of the solar cycle 23 and investigated the modeling bias for fast and slow solar winds. We find that the Helio1D pipeline performs best during the declining phase and solar minimum. However, the Helio1D pipeline often underestimates the speed of the fast wind while overestimates the speed of the slow wind, especially between the late declining phase and early ascending phase of the solar cycle 23. Furthermore, the solar wind structures modeled by Helio1D often arrives earlier than the observations especially for the fast wind. These caveats plausibly arise from the simplistic assumptions in the 1D MHD model, comprising the limited dimensionality, the lack of dissipation, and the solar wind acceleration physics, for example. Nevertheless, the Helio1D pipeline models consistent CIR formation while remains computationally light, which is desirable for operational forecasting.

To transition from case-by-case benchmarking to operational solar wind forecasting, we implemented (1) the pipeline calibration to alleviate the over-compression at stream interface due to the ideal MHD assumption, (2) the ensemble modeling of 21 solar wind solutions at virtual targets including the sub-Earth point to provide timing and magnitude uncertainties, and (3) the procedures to remove unphysical data points and automatically fill data gaps. The latter two procedures were discussed to be crucial in providing continuous, reliable service while providing forecasting uncertainties. Alternatively, the Helio1D pipeline can be adapted to use other more reliable magnetogram sources and with higher resolution, e.g., from Air Force Data Assimilative Photospheric Flux Transport [ADAPT; Hickmann et al., 2015, Arge et al., 2013, Worden and Harvey, 2000]. We emphasized that the implementation of procedures for making the pipeline fully operational, in addition to the pipeline benchmarking, are critical and they must be further tested in several situations before employing the pipeline for real applications.

Acknowledgements

The SafeSpace project has received funding from the European Union’s Horizon 2020 research and innovation programme under grant agreement No 870437. The 1D MHD model of solar wind propagation initially developed by Tao et al. [2005] and used for Helio1D is duplicated from the Heliopropa service provided by CDP (http://heliopropa.irap.omp.eu) and developed during the Planetary Space Weather Services (PSWS) Virtual Activity of the Europlanet H2020 Research Infrastructure funded by the European Union’s Horizon 2020 research and innovation programme under grant agreement No 654208 and extended during the Sun Planet Interactions Digital Environment on Request (SPIDER) Virtual Activity of the Europlanet H2024 Research Infrastructure funded by the European Union’s Horizon 2020 research and innovation programme under grant agreement No 871149. Work at IRAP is supported by the French National Centre for Scientific Research (CNRS), Centre national d’études spatiales (CNES), and the University of Toulouse III (UPS).

References

- A. G. Burns, S. C. Solomon, L. Qian, W. Wang, B. A. Emery, M. Wiltberger, and D. R. Weimer. The effects of Corotating interaction region/High speed stream storms on the thermosphere and ionosphere during the last solar minimum. *Journal of Atmospheric and Solar-Terrestrial Physics*, 83:79–87, July 2012. doi:10.1016/j.jastp.2012.02.006.
- I. G. Richardson, E. W. Cliver, and H. V. Cane. Sources of geomagnetic storms for solar minimum and maximum conditions during 1972–2000. *Geophysical Research Letters*, 28(13):2569–2572, 2001. doi:10.1029/2001GL013052.
- M. V. Alves, E. Echer, and W. D. Gonzalez. Geoeffectiveness of corotating interaction regions as measured by Dst index. *Journal of Geophysical Research (Space Physics)*, 111(A7):A07S05, July 2006. doi:10.1029/2005JA011379.
- Bruce T. Tsurutani, Walter D. Gonzalez, Alicia L. C. Gonzalez, Fernando L. Guarnieri, Nat Gopalswamy, Manuel Grande, Yohsuke Kamide, Yoshiya Kasahara, Gang Lu, Ian Mann, Robert McPherron, Finn Soraas, and Vytienis Vasyliunas. Corotating solar wind streams and recurrent geomagnetic activity: A review. *Journal of Geophysical Research (Space Physics)*, 111(A7):A07S01, July 2006. doi:10.1029/2005JA011273.
- Y. Zhang, W. Sun, X. S. Feng, C. S. Deehr, C. D. Fry, and M. Dryer. Statistical analysis of corotating interaction regions and their geoeffectiveness during solar cycle 23. *Journal of Geophysical Research (Space Physics)*, 113(A8):A08106, August 2008. doi:10.1029/2008JA013095.
- E. K. J. Kilpua, A. Balogh, R. von Steiger, and Y. D. Liu. Geoeffective properties of solar transients and stream interaction regions. *Space Science Reviews*, 212(3):1271–1314, 2017. doi:10.1007/s11214-017-0411-3.
- Yutian Chi, Chenglong Shen, Bingxian Luo, Yuming Wang, and Mengjiao Xu. Geoeffectiveness of stream interaction regions from 1995 to 2016. *Space Weather*, 16(12):1960–1971, 2018. doi:10.1029/2018SW001894.
- Oluwole J. Oyedokun, P. O. Amaechi, A. O. Akala, K. G. Simi, Aghogho Ogwala, and E. O. Oyeyemi. Solar and interplanetary events that drove two CIR-related geomagnetic storms of 1 June 2013 and 7 October 2015, and their ionospheric responses at the American and African equatorial ionization Anomaly regions. *Advances in Space Research*, 69(5):2168–2181, March 2022. doi:10.1016/j.asr.2021.12.027.
- S. Chakraborty, S. Ray, D. Sur, A. Datta, and A. Paul. Effects of CME and CIR induced geomagnetic storms on low-latitude ionization over Indian longitudes in terms of neutral dynamics. *Advances in Space Research*, 65(1):198–213, January 2020. doi:10.1016/j.asr.2019.09.047.
- Yousheng Liu, Fang Shen, and Yi Yang. Numerical Simulation on the Propagation and Deflection of Fast Coronal Mass Ejections (CMEs) Interacting with a Corotating Interaction Region in Interplanetary Space. *The Astrophysical Journal*, 887(2):150, December 2019. doi:10.3847/1538-4357/ab543e.
- Lulu Zhao, Gang Li, R. W. Ebert, M. A. Dayeh, M. I. Desai, G. M. Mason, Z. Wu, and Y. Chen. Modeling transport of energetic particles in corotating interaction regions: A case study. *Journal of Geophysical Research (Space Physics)*, 121(1):77–92, January 2016. doi:10.1002/2015JA021762.
- N. Wijsen, A. Aran, J. Pomoell, and S. Poedts. Interplanetary spread of solar energetic protons near a high-speed solar wind stream. *The Astrophysical Journal*, 624:A47, April 2019. doi:10.1051/0004-6361/201935139.
- N. Iucci, M. Parisi, M. Storini, and G. Villaresi. The Origin of Transient Cosmic-Ray Intensity Variations. In *International Cosmic Ray Conference*, volume 3 of *International Cosmic Ray Conference*, page 438, January 1979.
- A. P. Rouillard and M. Lockwood. The Latitudinal Effect of Corotating Interaction Regions on Galactic Cosmic Rays. *Solar Physics*, 245(1):191–206, September 2007. doi:10.1007/s11207-007-9019-1.
- Steven R. Cranmer, Sarah E. Gibson, and Pete Riley. Origins of the Ambient Solar Wind: Implications for Space Weather. *Space Science Reviews*, 212(3-4):1345–1384, November 2017. doi:10.1007/s11214-017-0416-y.

- Bojan Vršnak, Mateja Dumbović, Jaša Čalogović, Giuliana Verbanac, and Ivana Poljančić Beljan. Geomagnetic Effects of Corotating Interaction Regions. *Solar Physics*, 292(9):140, September 2017. doi:10.1007/s11207-017-1165-5.
- Ian G. Richardson. Solar wind stream interaction regions throughout the heliosphere. *Living Reviews in Solar Physics*, 15(1):1, January 2018. doi:10.1007/s41116-017-0011-z.
- Yu. I. Yermolaev, I. G. Lodkina, N. S. Nikolaeva, M. Yu. Yermolaev, M. O. Riazantseva, and L. S. Rakhmanova. Statistic study of the geoeffectiveness of compression regions CIRs and Sheaths. *Journal of Atmospheric and Solar-Terrestrial Physics*, 180:52–59, November 2018. doi:10.1016/j.jastp.2018.01.027.
- M. M. Lam, R. B. Horne, N. P. Meredith, and S. A. Glauert. Radiation belt electron flux variability during three CIR-driven geomagnetic storms. *Journal of Atmospheric and Solar-Terrestrial Physics*, 71(10-11):1145–1156, July 2009. doi:10.1016/j.jastp.2008.06.007.
- Mary K. Hudson, Scot R. Elkington, Zhao Li, Maulik Patel, Kevin Pham, Kareem Sorathia, Alex Boyd, Allison Jaynes, and Alexis Leali. MHD-Test Particles Simulations of Moderate CME and CIR-Driven Geomagnetic Storms at Solar Minimum. *Space Weather*, 19(12):e02882, December 2021. doi:10.1029/2021SW002882.
- J. B. Blake, D. N. Baker, N. Turner, K. W. Ogilvie, and R. P. Lepping. Correlation of changes in the outer-zone relativistic-electron population with upstream solar wind and magnetic field measurements. *Geophysical Research Letters*, 24(8):927–929, April 1997. doi:10.1029/97GL00859.
- Xinlin Li, D. N. Baker, M. Temerin, D. Larson, R. P. Lin, G. D. Reeves, M. Looper, S. G. Kanekal, and R. A. Mewaldt. Are energetic electrons in the solar wind the source of the outer radiation belt? *Geophysical Research Letters*, 24(8): 923–926, April 1997. doi:10.1029/97GL00543.
- G. A. Paulikas and J. B. Blake. Effects of the solar wind on magnetospheric dynamics: Energetic electrons at the synchronous orbit. *Geophysical Monograph Series*, 21:180–202, January 1979. doi:10.1029/GM021p0180.
- Victor A. Pinto, Hee-Jeong Kim, Larry R. Lyons, and Jacob Bortnik. Interplanetary Parameters Leading to Relativistic Electron Enhancement and Persistent Depletion Events at Geosynchronous Orbit and Potential for Prediction. *Journal of Geophysical Research (Space Physics)*, 123(2):1134–1145, February 2018. doi:10.1002/2017JA024902.
- Megha Pandya, Veenadhari Bhaskara, Yusuke Ebihara, Shrikanth G. Kanekal, and Daniel N. Baker. Variation of radiation belt electron flux during cme- and cir-driven geomagnetic storms: Van allen probes observations. *Journal of Geophysical Research: Space Physics*, 124(8):6524–6540, 2019. doi:10.1029/2019JA026771.
- Richard B. Horne, Mark W. Phillips, Sarah A. Glauert, Nigel P. Meredith, Alex D. P. Hands, Keith A. Ryden, and Wen Li. Realistic Worst Case for a Severe Space Weather Event Driven by a Fast Solar Wind Stream. *Space Weather*, 16(9):1202–1215, September 2018. doi:10.1029/2018SW001948.
- Ch. Katsavrias, I. Sandberg, W. Li, O. Podladchikova, I.A. Daglis, C. Papadimitriou, C. Tsironis, and S. Aminalragia-Giamini. Highly relativistic electron flux enhancement during the weak geomagnetic storm of april–may 2017. *Journal of Geophysical Research: Space Physics*, 124(6):4402–4413, 2019. doi:10.1029/2019JA026743.
- Joseph E. Borovsky and Michael H. Denton. Differences between cme-driven storms and cir-driven storms. *Journal of Geophysical Research: Space Physics*, 111(A7), 2006. doi:10.1029/2005JA011447.
- Y. Miyoshi, R. Kataoka, Y. Kasahara, A. Kumamoto, T. Nagai, and M. F. Thomsen. High-speed solar wind with southward interplanetary magnetic field causes relativistic electron flux enhancement of the outer radiation belt via enhanced condition of whistler waves. *Geophysical Research Letters*, 40(17):4520–4525, 2013. doi:10.1002/grl.50916.
- Louis J. Lanzerotti. *Space weather effects on communications*, pages 247–268. Springer Berlin Heidelberg, Berlin, Heidelberg, 2007. ISBN 978-3-540-34578-7. doi:10.1007/978-3-540-34578-7_9.
- Richard B. Horne, Sarah A. Glauert, Nigel P. Meredith, Hannu Koskinen, Rami Vainio, Alexandr Afanasiev, Natalia Y. Ganushkina, Olga A. Amariutei, Daniel Boscher, Angelica Sicard, Vincent Maget, Stefaan Poedts, Carla Jacobs, Blai Sanahuja, Angels Aran, Daniel Heynderickx, and David Pitchford. Forecasting the Earth’s radiation belts and modelling solar energetic particle events: Recent results from SPACECAST. *Journal of Space Weather and Space Climate*, 3:A20, May 2013. doi:10.1051/swsc/2013042.
- C. N. Arge and V. J. Pizzo. Improvement in the prediction of solar wind conditions using near-real time solar magnetic field updates. *Journal of Geophysical Research: Space Physics*, 105(A5):10465–10480, May 2000. doi:10.1029/1999JA000262.
- C. N. Arge, J. G. Luhmann, D. Odstrcil, C. J. Schrijver, and Y. Li. Stream structure and coronal sources of the solar wind during the May 12th, 1997 CME. *Journal of Atmospheric and Solar-Terrestrial Physics*, 66(15-16):1295–1309, October 2004. doi:10.1016/j.jastp.2004.03.018.
- D. Odstrčil, M. Dryer, and Z. Smith. Propagation of an interplanetary shock along the heliospheric plasma sheet. *Journal of Geophysical Research: Space Physics*, 101(A9):19973–19986, September 1996. doi:10.1029/96JA00479.

- D. Odstrcil and V. J. Pizzo. Distortion of the interplanetary magnetic field by three-dimensional propagation of coronal mass ejections in a structured solar wind. *Journal of Geophysical Research: Space Physics*, 104(A12):28225–28240, January 1999. doi:10.1029/1999JA900319.
- Dusan Odstrcil, Victor J. Pizzo, Jon A. Linker, Pete Riley, Roberto Lionello, and Zoran Mikic. Initial coupling of coronal and heliospheric numerical magnetohydrodynamic codes. *Journal of Atmospheric and Solar-Terrestrial Physics*, 66(15-16):1311–1320, October 2004. doi:10.1016/j.jastp.2004.04.007.
- A. Taktakishvili, M. Kuznetsova, P. MacNeice, M. Hesse, L. Rastätter, A. Pulkkinen, A. Chulaki, and D. Odstrcil. Validation of the coronal mass ejection predictions at the Earth orbit estimated by ENLIL heliosphere cone model. *Space Weather*, 7(3):S03004, March 2009. doi:10.1029/2008SW000448.
- A. Taktakishvili, A. Pulkkinen, P. MacNeice, M. Kuznetsova, M. Hesse, and D. Odstrcil. Modeling of coronal mass ejections that caused particularly large geomagnetic storms using ENLIL heliosphere cone model. *Space Weather*, 9(6):06002, June 2011. doi:10.1029/2010SW000642.
- Aleksandre Taktakishvili, L. Mays, K. Manoharan, L. Rastaetter, and M. Kuznetsova. Using Interplanetary Scintillation Data to Improve Ensemble Modeling of Coronal Mass Ejections. In *Solar Heliospheric and Interplanetary Environment (SHINE 2018)*, page 120, July 2018.
- Vic Pizzo, George Millward, Annette Parsons, Douglas Biesecker, Steve Hill, and Dusan Odstrcil. Wang-Sheeley-Arge-Enlil Cone Model Transitions to Operations. *Space Weather*, 9(3):03004, March 2011. doi:10.1029/2011SW000663.
- J. A. Linker, Z. Mikić, D. A. Biesecker, R. J. Forsyth, S. E. Gibson, A. J. Lazarus, A. Lecinski, P. Riley, A. Szabo, and B. J. Thompson. Magnetohydrodynamic modeling of the solar corona during Whole Sun Month. *Journal of Geophysical Research: Space Physics*, 104(A5):9809–9830, May 1999. doi:10.1029/1998JA900159.
- Pete Riley, Jon A. Linker, R. Lionello, and Z. Mikic. Corotating interaction regions during the recent solar minimum: The power and limitations of global MHD modeling. *Journal of Atmospheric and Solar-Terrestrial Physics*, 83:1–10, July 2012. doi:10.1016/j.jastp.2011.12.013.
- M. J. Owens, C. N. Arge, H. E. Spence, and A. Pembroke. An event-based approach to validating solar wind speed predictions: High-speed enhancements in the Wang-Sheeley-Arge model. *Journal of Geophysical Research (Space Physics)*, 110(A12):A12105, December 2005. doi:10.1029/2005JA011343.
- C. O. Lee, J. G. Luhmann, D. Odstrcil, P. J. MacNeice, I. de Pater, P. Riley, and C. N. Arge. The Solar Wind at 1 AU During the Declining Phase of Solar Cycle 23: Comparison of 3D Numerical Model Results with Observations. *Solar Physics*, 254(1):155–183, January 2009. doi:10.1007/s11207-008-9280-y.
- Peter MacNeice. Validation of community models: Identifying events in space weather model timelines. *Space Weather*, 7(6):S06004, June 2009a. doi:10.1029/2009SW000463.
- Peter MacNeice. Validation of community models: 2. Development of a baseline using the Wang-Sheeley-Arge model. *Space Weather*, 7(12):S12002, December 2009b. doi:10.1029/2009SW000489.
- L. K. Jian, C. T. Russell, J. G. Luhmann, P. J. MacNeice, D. Odstrcil, P. Riley, J. A. Linker, R. M. Skoug, and J. T. Steinberg. Comparison of Observations at ACE and Ulysses with Enlil Model Results: Stream Interaction Regions During Carrington Rotations 2016 - 2018. *Solar Physics*, 273(1):179–203, October 2011a. doi:10.1007/s11207-011-9858-7.
- L. K. Jian, C. T. Russell, and J. G. Luhmann. Comparing Solar Minimum 23/24 with Historical Solar Wind Records at 1 AU. *Solar Physics*, 274(1-2):321–344, December 2011b. doi:10.1007/s11207-011-9737-2.
- L. K. Jian, P. J. MacNeice, A. Taktakishvili, D. Odstrcil, B. Jackson, H. S. Yu, P. Riley, I. V. Sokolov, and R. M. Evans. Validation for solar wind prediction at Earth: Comparison of coronal and heliospheric models installed at the CCMC. *Space Weather*, 13(5):316–338, May 2015. doi:10.1002/2015SW001174.
- P. Riley and R. Lionello. Mapping Solar Wind Streams from the Sun to 1 AU: A Comparison of Techniques. *Solar Physics*, 270(2):575–592, June 2011. doi:10.1007/s11207-011-9766-x.
- M. Dósa, A. Opitz, Z. Dály, and K. Szegő. Magnetic lasso: A new kinematic solar wind propagation method. *Solar Physics*, 293(9):127, 2018. doi:10.1007/s11207-018-1340-3.
- Martin A. Reiss, Peter J. MacNeice, Karin Muglach, Charles N. Arge, Christian Möstl, Pete Riley, Jürgen Hinterreiter, Rachel L. Bailey, Andreas J. Weiss, Mathew J. Owens, Tanja Amerstorfer, and Ute Amerstorfer. Forecasting the Ambient Solar Wind with Numerical Models. II. An Adaptive Prediction System for Specifying Solar Wind Speed near the Sun. *The Astrophysical Journal*, 891(2):165, March 2020. doi:10.3847/1538-4357/ab78a0.
- P. MacNeice, L. K. Jian, S. K. Antiochos, C. N. Arge, C. D. Bussy-Virat, M. L. DeRosa, B. V. Jackson, J. A. Linker, Z. Mikic, M. J. Owens, A. J. Ridley, P. Riley, N. Savani, and I. Sokolov. Assessing the quality of models of the ambient solar wind. *Space Weather*, 16(11):1644–1667, 2018. doi:10.1029/2018SW002040.

- Martin A. Reiss, Peter J. MacNeice, Leila M. Mays, Charles N. Arge, Christian Möstl, Ljubomir Nikolic, and Tanja Amerstorfer. Forecasting the Ambient Solar Wind with Numerical Models. I. On the Implementation of an Operational Framework. *The Astrophysical Journal*, 240(2):35, February 2019. doi:10.3847/1538-4365/aaf8b3.
- Rui F. Pinto and Alexis P. Rouillard. A Multiple Flux-tube Solar Wind Model. *The Astrophysical Journal*, 838(2):89, April 2017. doi:10.3847/1538-4357/aa6398.
- A. P. Rouillard, R. F. Pinto, A. Vourlidas, A. De Groof, W. T. Thompson, A. Bemporad, S. Dolei, M. Indurain, E. Buchlin, C. Sasso, D. Spadaro, K. Dalmasse, J. Hirzberger, I. Zouganelis, A. Strugarek, A. S. Brun, M. Alexandre, D. Berghmans, N. E. Raouafi, T. Wiegmann, P. Pagano, C. N. Arge, T. Nieves-Chinchilla, M. Lavarra, N. Poirier, T. Amari, A. Aran, V. Andretta, E. Antonucci, A. Anastasiadis, F. Auchère, L. Bellot Rubio, B. Nicula, X. Bonnin, M. Bouchemit, E. Budnik, S. Caminade, B. Cecconi, J. Carlyle, I. Cernuda, J. M. Davila, L. Etesi, F. Espinosa Lara, A. Fedorov, S. Fineschi, A. Fludra, V. Génot, M. K. Georgoulis, H. R. Gilbert, A. Giunta, R. Gomez-Herrero, S. Guest, M. Haberreiter, D. Hassler, C. J. Henney, R. A. Howard, T. S. Horbury, M. Janvier, S. I. Jones, K. Kozarev, E. Kraaikamp, A. Kouloumvakos, S. Krucker, A. Lagg, J. Linker, B. Lavraud, P. Louarn, M. Maksimovic, S. Maloney, G. Mann, A. Masson, D. Müller, H. Önel, P. Osuna, D. Orozco Suarez, C. J. Owen, A. Papaioannou, D. Pérez-Suárez, J. Rodriguez-Pacheco, S. Parenti, E. Pariat, H. Peter, S. Plunkett, J. Pomoell, J. M. Raines, T. L. Riethmüller, N. Rich, L. Rodriguez, M. Romoli, L. Sanchez, S. K. Solanki, O. C. St Cyr, T. Straus, R. Susino, L. Teriaca, J. C. del Toro Iniesta, R. Ventura, C. Verbeeck, N. Vilmer, A. Warmuth, A. P. Walsh, C. Watson, D. Williams, Y. Wu, and A. N. Zhukov. Models and data analysis tools for the Solar Orbiter mission. *Astronomy and Astrophysics*, 642:A2, October 2020. doi:10.1051/0004-6361/201935305.
- Jens Pomoell and S. Poedts. EUHFORIA: European heliospheric forecasting information asset. *Journal of Space Weather and Space Climate*, 8:A35, June 2018. doi:10.1051/swsc/2018020.
- E. Samara, R. F. Pinto, J. Magdalenic, N. Wijzen, V. Jerčić, C. Scolini, I. C. Jebaraj, L. Rodriguez, and S. Poedts. Implementing the MULTI-VP coronal model in EUHFORIA: Test case results and comparisons with the WSA coronal model. *Astronomy and Astrophysics*, 648:A35, April 2021. doi:10.1051/0004-6361/202039325.
- Jürgen Hinterreiter, Jasmina Magdalenic, Manuela Temmer, Christine Verbeke, Immanuel Christopher Jebaraj, Evangelia Samara, Eleanna Asvestari, Stefaan Poedts, Jens Pomoell, Emilia Kilpua, Luciano Rodriguez, Camilla Scolini, and Alexey Isavnin. Assessing the Performance of EUHFORIA Modeling the Background Solar Wind. *Solar Physics*, 294(12):170, December 2019. doi:10.1007/s11207-019-1558-8.
- E. Samara, B. Laperre, R. Kieokaew, M. Temmer, C. Verbeke, L. Rodriguez, J. Magdalenic, and S. Poedts. Dynamic Time Warping as a Means of Assessing Solar Wind Time Series. *The Astrophysical Journal*, 927(2):187, March 2022. doi:10.3847/1538-4357/ac4af6.
- Bojan Vršnak, Manuela Temmer, and Astrid M. Veronig. Coronal Holes and Solar Wind High-Speed Streams: I. Forecasting the Solar Wind Parameters. *Solar Physics*, 240(2):315–330, February 2007. doi:10.1007/s11207-007-0285-8.
- Daniel Milošić, Manuela Temmer, and Stephan G. Heinemann. Improving the empirical solar wind forecast (eswf) - compression effects, co-latitude infor- improving the empirical solar wind forecast - compression effects, co-latitude information, and dst forecasting. Master's thesis, University of Graz, July 2022.
- S. Robbins, C. J. Henney, and J. W. Harvey. Solar Wind Forecasting with Coronal Holes. *Solar Physics*, 233(2): 265–276, February 2006. doi:10.1007/s11207-006-0064-y.
- Chihiro Tao, Ryuho Kataoka, Hiroshi Fukunishi, Yukihiro Takahashi, and Takaaki Yokoyama. Magnetic field variations in the Jovian magnetotail induced by solar wind dynamic pressure enhancements. *Journal of Geophysical Research (Space Physics)*, 110(A11):A11208, November 2005. doi:10.1029/2004JA010959.
- N. André, M. Grande, N. Achilleos, M. Barthélémy, M. Bouchemit, K. Benson, P.-L. Blelly, E. Budnik, S. Caussarieu, B. Cecconi, T. Cook, V. Génot, P. Guio, A. Goutenoir, B. Grison, R. Hueso, M. Indurain, G.H. Jones, J. Liliensten, A. Marchaudon, D. Matthäi, A. Opitz, A. Rouillard, I. Stanislawska, J. Soucek, C. Tao, L. Tomasik, and J. Vaubailon. Virtual planetary space weather services offered by the europlanet h2020 research infrastructure. *Planetary and Space Science*, 150:50–59, 2018. ISSN 0032-0633. doi:https://doi.org/10.1016/j.pss.2017.04.020. Enabling Open and Interoperable Access to Planetary Science and Heliophysics Databases and Tools.
- Frank Woodcock. The evaluation of yes/no forecasts for scientific and administrative purposes. *Monthly Weather Review*, 104(10):1209–1214, 1976.
- Martin A. Reiss, Manuela Temmer, Astrid M. Veronig, Ljubomir Nikolic, Susanne Vennerstrom, Florian Schöngassner, and Stefan J. Hofmeister. Verification of high-speed solar wind stream forecasts using operational solar wind models. *Space Weather*, 14(7):495–510, July 2016. doi:10.1002/2016SW001390.

- Yosuke Matsumoto, Yuta Asahina, Yuki Kudoh, Tomohisa Kawashima, Jin Matsumoto, Hiroyuki R. Takahashi, Takashi Minoshima, Seiji Zenitani, Takahiro Miyoshi, and Ryoji Matsumoto. Magnetohydrodynamic simulation code CANS+: Assessments and applications. *Publications of the Astronomical Society of Japan*, 71(4):83, August 2019. doi:10.1093/pasj/psz064.
- Erika Palmerio, Teresa Nieves-Chinchilla, Emilia K. J. Kilpua, David Barnes, Andrei N. Zhukov, Lan K. Jian, Olivier Witasse, Gabrielle Provan, Chihiro Tao, Laurent Lamy, Thomas J. Bradley, M. Leila Mays, Christian Möstl, Elias Roussos, Yoshifumi Futaana, Adam Masters, and Beatriz Sánchez-Cano. Magnetic Structure and Propagation of Two Interacting CMEs From the Sun to Saturn. *Journal of Geophysical Research (Space Physics)*, 126(11): e2021JA029770, November 2021. doi:10.1029/2021JA029770.
- H. Nilsson, A. Moeslinger, H. N. Williamson, S. Bergman, H. Gunell, G. Stenberg Wieser, Y. Futaana, T. Karlsson, E. Behar, and M. Holmström. Upstream solar wind speed at comet 67P. Reconstruction method, model comparison, and results. *Astronomy and Astrophysics*, 659:A18, March 2022. doi:10.1051/0004-6361/202142867.
- J. H. King and N. E. Papitashvili. Solar wind spatial scales in and comparisons of hourly Wind and ACE plasma and magnetic field data. *Journal of Geophysical Research (Space Physics)*, 110(A2):A02104, February 2005. doi:10.1029/2004JA010649.
- M. Müller. Dynamic Time Warping. In *Information Retrieval for Music and Motion*, pages 69–84. Springer Berlin Heidelberg, Berlin, Heidelberg, 2007. ISBN 978-3-540-74048-3. doi:10.1007/978-3-540-74048-3_4.
- R. Bellman and R. Kalaba. On adaptive control processes. *IRE Transactions on Automatic Control*, 4(2):1–9, 1959. doi:10.1109/TAC.1959.1104847.
- H. Sakoe and S. Chiba. Dynamic programming algorithm optimization for spoken word recognition. *IEEE Transactions on Acoustics, Speech, and Signal Processing*, 26(1):43–49, 1978. doi:10.1109/TASSP.1978.1163055.
- C. Myers, L. Rabiner, and A. Rosenberg. Performance tradeoffs in dynamic time warping algorithms for isolated word recognition. *IEEE Transactions on Acoustics, Speech, and Signal Processing*, 28(6):623–635, 1980. doi:10.1109/TASSP.1980.1163491.
- Brecht Laperre, Jorge Amaya, and Giovanni Lapenta. Dynamic Time Warping as a New Evaluation for Dst Forecast with Machine Learning. *Frontiers in Astronomy and Space Sciences*, 7:39, July 2020. doi:10.3389/fspas.2020.00039.
- Mathew J. Owens and Jonathan D. Nichols. Using in situ solar-wind observations to generate inner-boundary conditions to outer-heliosphere simulations - I. Dynamic time warping applied to synthetic observations. *Monthly Notices of Royal Astronomical Society*, 508(2):2575–2582, December 2021. doi:10.1093/mnras/stab2512.
- Kaine A. Bunting and Huw Morgan. An inner boundary condition for solar wind models based on coronal density. *Journal of Space Weather and Space Climate*, 12:30, July 2022. doi:10.1051/swsc/2022026.
- D. Berndt and J. Clifford. Using dynamic time warping to find patterns in time series. Technical report, AAAI-94 Workshop on Knowledge Discovery in Databases, 1994.
- Eamonn J. Keogh and Michael J. Pazzani. Derivative Dynamic Time Warping. In *Proceedings of the 2001 SIAM International Conference on Data Mining*, pages 1–11. Society for Industrial and Applied Mathematics, April 2001. ISBN 978-0-89871-495-1 978-1-61197-271-9. doi:10.1137/1.9781611972719.1.
- Tomasz Górecki and Maciej Łuczak. Using derivatives in time series classification. *Data Mining and Knowledge Discovery*, 26(2):310–331, 2013. doi:10.1007/s10618-012-0251-4.
- Selina Chu, Eamonn Keogh, David Hart, and Michael Pazzani. *Iterative Deepening Dynamic Time Warping for Time Series*, pages 195–212. Society for Industrial and Applied Mathematics, 2002. doi:10.1137/1.9781611972726.12.
- Eamonn Keogh and Chotirat Ann Ratanamahatana. Exact indexing of dynamic time warping. *Knowledge and Information Systems*, 7(3):358–386, 2005. doi:10.1007/s10115-004-0154-9.
- Stan Salvador and Philip Chan. Toward accurate dynamic time warping in linear time and space. *Intelligent Data Analysis*, 11(5):561–580, oct 2007. ISSN 15714128. doi:10.3233/IDA-2007-11508.
- Alon Efrat, Quanfu Fan, and Suresh Venkatasubramanian. Curve matching, time warping, and light fields: New algorithms for computing similarity between curves. *Journal of Mathematical Imaging and Vision*, 27(3):203–216, 2007. doi:10.1007/s10851-006-0647-0.
- Titus Felix Furtună. Dynamic programming algorithms in speech recognition. *Revista Informatica Economică nr. 2* (46):94, 2008.
- Qiang Zhu, Gustavo Batista, Thanawin Rakthanmanon, and Eamonn Keogh. A novel approximation to dynamic time warping allows anytime clustering of massive time series datasets. In *Proceedings of the 2012 SIAM international conference on data mining*, pages 999–1010. SIAM, 2012.

- Munshi Yadav and M Afshar Alam. Dynamic time warping (dtw) algorithm in speech: a review. *International Journal of Research in Electronics and Computer Engineering*, 6(1):524–528, 2018.
- Bertalan Zieger and Kenneth C. Hansen. Statistical validation of a solar wind propagation model from 1 to 10 AU. *Journal of Geophysical Research: Space Physics*, 113(A8):n/a–n/a, aug 2008. ISSN 01480227. doi:10.1029/2008JA013046.
- Mathew J. Owens and Pete Riley. Probabilistic Solar Wind Forecasting Using Large Ensembles of Near-Sun Conditions With a Simple One-Dimensional “Upwind” Scheme. *Space Weather*, 15(11):1461–1474, November 2017. doi:10.1002/2017SW001679.
- V. Pizzo. A three-deminsional model of corotating streams in the solar wind 1. Theoretical foundations. *Journal of Geophysical Research: Space Physics*, 83(A12):5563–5572, December 1978. doi:10.1029/JA083iA12p05563.
- Rainer Schwenn. *Large-Scale Structure of the Interplanetary Medium*, pages 99–181. Springer Berlin Heidelberg, Berlin, Heidelberg, 1990. ISBN 978-3-642-75361-9. doi:10.1007/978-3-642-75361-9_3.
- Kyle S. Hickmann, Humberto C. Godinez, Carl J. Henney, and C. Nick Arge. Data Assimilation in the ADAPT Photospheric Flux Transport Model. *Solar Physics*, 290(4):1105–1118, April 2015. doi:10.1007/s11207-015-0666-3.
- C. Nick Arge, Carl J. Henney, Irene Gonzalez Hernandez, W. Alex Toussaint, Josef Koller, and Humberto C. Godinez. Modeling the corona and solar wind using ADAPT maps that include far-side observations. In Gary P. Zank, Joe Borovsky, Roberto Bruno, Jonathan Cirtain, Steve Cranmer, Heather Elliott, Joe Giacalone, Walter Gonzalez, Gang Li, Eckart Marsch, Ebehard Moebius, Nick Pogorelov, Jim Spann, and Olga Verkhoglyadova, editors, *Solar Wind 13*, volume 1539 of *American Institute of Physics Conference Series*, pages 11–14, June 2013. doi:10.1063/1.4810977.
- John Worden and John Harvey. An Evolving Synoptic Magnetic Flux map and Implications for the Distribution of Photospheric Magnetic Flux. *Solar Physics*, 195(2):247–268, August 2000. doi:10.1023/A:1005272502885.